Intermediate-mass-ratio black hole binaries: Intertwining numerical and perturbative techniques

Carlos O. Lousto, Hiroyuki Nakano, Yosef Zlochower, and Manuela Campanelli

Center for Computational Relativity and Gravitation and School of Mathematical Sciences, Rochester Institute of Technology,
85 Lomb Memorial Drive, Rochester, New York 14623, USA

We describe in detail full numerical and perturbative techniques to compute the gravitational radiation from intermediate-mass-ratio black-hole-binary inspirals and mergers. We perform a series of full numerical simulations of nonspinning black holes with mass ratios $q = 1/10$ and $q = 1/15$ from different initial separations and for different finite-difference resolutions. In order to perform those full numerical runs, we adapt the gauge of the moving punctures approach with a variable damping term for the shift. We also derive an extrapolation (to infinite radius) formula for the waveform extracted at finite radius. For the perturbative evolutions we use the full numerical tracks, transformed into the Schwarzschild gauge, in the source terms of the Regge-Wheeler-Zerilli Schwarzschild perturbations formalism. We then extend this perturbative formalism to take into account small intrinsic spins of the large black hole, and validate it by computing the quasinormal mode frequencies, where we find good agreement for spins $|a/M| < 0.3$. Including the final spins improves the overlap functions when comparing full numerical and perturbative waveforms, reaching 99.5% for the leading $(\ell, m) = (2, 2)$ and $(3, 3)$ modes, and 98.3% for the nonleading $(2, 1)$ mode in the $q = 1/10$ case, which includes 8 orbits before merger. For the $q = 1/15$ case, we obtain overlaps near 99.7% for all three modes. We discuss the modeling of the full inspiral and merger based on a combined matching of post-Newtonian, full numerical, and geodesic trajectories.

I. INTRODUCTION

There is strong indirect evidence for the existence of black holes (BHs) of a few solar masses ($M_\odot$) residing in galaxies and for supermassive BHs (SMBHs), with masses 10^5–$10^{10} M_\odot$ in the central cores of active galaxies. These BHs can form binaries, and the mergers of black-hole binaries (BHBs) are expected to be the strongest sources of gravitational radiation and the most energetic event in the Universe. The current generation of ground-based interferometric gravitational wave detectors, such as LIGO, VIRGO, and GEO, are most sensitive to BHB mergers with total masses of a few tens to hundreds of solar masses, while the space-based LISA detector will be sensitive to mergers of BHBs with a few million solar masses.

The existence of intermediate-mass BHs (IMBH), from a few hundred to tens of thousand of solar masses, is still uncertain. If they exist, then these IMBH can form binaries with solar-mass-sized objects, leading to compact-object mergers with mass ratios in the range $0.001 < q = m_1/m_2 < 0.1$, which could be detected by advanced LIGO. The detection of gravitational waves from these encounters, as well as the correct modeling of the waveform as a function of the BHBs' physical parameters, would allow us to estimate the population of such objects in the Universe. Likewise, encounters of IMBH with SMBHs in the centers of galaxies would lead to mergers with mass ratios in the range $0.001 < q < 0.1$, detectable by LISA. On the other hand, theoretical N-body simulations [1], assuming direct cosmological collisions of galaxies with central SMBHs, set the most likely SMBH binary-mass ratios in the range $0.01 < q < 0.1$.

In Refs. [2,3], the prospects of detecting IMBH binary (IMBHB) inspirals with advanced LIGO was discussed, and in Ref. [4], it was shown that intermediate-mass-ratio (IMR) inspirals of IMBHs plunging into supermassive BHs would be relevant to LISA, while IMR mergers of IMBHs with stellar objects can be detected by LIGO/VIRGO. In both cases the accuracy of the post-Newtonian (PN) approach (which was used to model the gravitational radiation) was questioned and the need for more accurate waveforms was stressed.

After the 2005 breakthroughs in numerical relativity [5–7], simulations of BHBs became routine. The exploration of generic binaries [8] led to the discovery of large recoils acquired by the remnant BH. While long-term generic BHB evolutions are possible, including the last few tens of orbits [9,10], two very interesting corners of the intrinsic parameter space of the BHBs remain largely unexplored: maximally spinning binaries and the small mass ratio limit.

In a previous paper [11], we introduced a new technique that makes use of nonlinear numerical trajectories and efficient perturbative evolutions to compute waveforms at large radii for the leading and nonleading modes. As a proof-of-concept, we computed waveforms for a relatively close binary with $q = 1/10$. In this paper we will describe these techniques in detail, extend them to slowly spinning black holes, and reach smaller mass ratios, to the $q = 1/15$ case, with full numerical simulations.

The paper is organized as follows. In Sec. II we describe the full numerical techniques employed in the evolution of BHBs. Those are based in the moving puncture approach [5,6] with a gauge choice that allows a spatial and time variation of the gamma-driver parameter $\eta(x^a, t)$. We describe the results of the simulations for two different mass ratios $q = 1/10, 1/15$ and two different initial separations leading to evolutions with BHs performing between 4 and 8 orbits prior to merger, the latter representing the longest waveform published so far in the small q regime. The gauge has also been shown to work for evolutions of a nonspinning $q = 1/100$ BHB [12]. In Sec. III we describe the perturbative techniques used to evolve a particle around a massive black hole. We extend the Regge-Wheeler-Zerilli (RWZ) techniques to include, perturbatively, a term linear in the spin of the larger black hole. This takes the form of second-order perturbations and adds a source term to the usual Schwarzschild perturbations (spin RWZ, noted hereafter as SRWZ). We also study the asymptotic behavior of the perturbative solutions for large r and come up with a practical way of correcting finite observer location effects perturbatively on the numerical waveforms. In Sec. IV we describe the results of comparing full numerical waveforms with perturbative ones that use the full numerical tracks for the particle motion. We compute matching overlaps for the leading modes $(\ell, m) = (2, 2)$; $(2, 1)$; $(3, 3)$. We verify the scaling of the waveform amplitudes with the reduced mass μ for the mass ratios $q = 1/10$, $1/15$. We also quantify the effects of adding the spin of the final black hole into the perturbative integrations. In Sec. V we discuss the properties of the full numerical trajectories in the two cases studied, $q = 1/10, 1/15$, that can be generalized to smaller mass ratios and hence can help in providing a modeling for the tracks used in the perturbative integrations, in particular, the final "universal plunge" and the use of resummed PN trajectories for the stages prior to the full numerical simulation. Finally, in the Appendix we give further evidence of the accuracy and validity of the SRWZ formalism here developed by computing the quasinormal modes and comparing them with the exact Kerr black-hole modes for different values of the spin parameter.

II. NUMERICAL RELATIVITY TECHNIQUES

To compute the numerical initial data, we use the puncture approach [13] along with the TWO PUNCTURES [14] thorn. In this approach the 3-metric on the initial slice has the form $\gamma_{ab} = (\psi_{BL} + u)^4 \delta_{ab}$, where ψ_{BL} is the Brill-Lindquist conformal factor, δ_{ab} is the Euclidean metric, and u is (at least) C^2 on the punctures. The Brill-Lindquist conformal factor is given by $\psi_{BL} = 1 + \sum_{i=1}^n m_i^p/(2|\vec{r} - \vec{r}_i|)$, where n is the total number of "punctures", m_i^p is the mass parameter of puncture i (m_i^p is *not* the horizon mass associated with puncture i), and $\vec{r}_i$ is the coordinate location of puncture i. We evolve these black-hole-binary

data-sets using the LAZEV [15] implementation of the moving puncture approach [5,6] with the conformal factor $W = \sqrt{\chi} = \exp(-2\phi)$ suggested by [16]. For the runs presented here we use centered, eighth-order finite differencing in space [17] and an RK4 time integrator. (Note that we do not upwind the advection terms.)

We use the CARPET [18] mesh refinement driver to provide a "moving-boxes" style of mesh refinement. In this approach, refined grids of fixed size are arranged about the coordinate centers of both holes. The CARPET code then moves these fine grids about the computational domain by following the trajectories of the two black holes.

We use AHFINDERDIRECT [19] to locate apparent horizons. We measure the magnitude of the horizon spin using the isolated horizon algorithm detailed in [20]. This algorithm is based on finding an approximate rotational Killing vector (i.e., an approximate rotational symmetry) on the horizon φ^a. Given this approximate Killing vector φ^a, the spin magnitude is

$$S_{[\varphi]} = \frac{1}{8\pi} \int_{AH} (\varphi^a R^b K_{ab}) d^2 V, \tag{1}$$

where K_{ab} is the extrinsic curvature of the 3D-slice, $d^2 V$ is the natural volume element intrinsic to the horizon, and R^a is the outward pointing unit vector normal to the horizon on the 3D-slice. We measure the direction of the spin by finding the coordinate line joining the poles of this Killing vector field using the technique introduced in [21]. Our algorithm for finding the poles of the Killing vector field has an accuracy of $\sim 2°$ (see [21] for details). Note that once we have the horizon spin, we can calculate the horizon mass via the Christodoulou formula,

$$m^H = \sqrt{m_{irr}^2 + S^2/(4 m_{irr}^2)}, \tag{2}$$

where $m_{irr} = \sqrt{A/(16\pi)}$ and A is the surface area of the horizon. We measure radiated energy, linear momentum, and angular momentum, in terms of ψ_4, using the formulae provided in Refs. [22,23]. However, rather than using the full ψ_4, we decompose it into ℓ and m modes and solve for the radiated linear momentum, dropping terms with $\ell \geq 5$. The formulae in Refs. [22,23] are valid at $r = \infty$. Typically, we would extract the radiated energy-momentum at finite radius and extrapolate to $r = \infty$. However, for the smaller mass ratios examined here, noise in the waveform introduces spurious effects that make these extrapolations inaccurate. We therefore use the average of these quantities extracted at radii $r = 70, 80, 90, 100$ and use the difference between these quantities at different radii as a measure of the error. We found that extrapolating the waveform itself to $r = \infty$ introduced phase errors due to uncertainties in the areal radius of the observers, as well as numerical noise. Thus when

comparing perturbative to numerical waveforms, we use the waveform extracted at $r = 100M$. In Sec. III B 7 we provide an alternative method of extrapolation of waveforms based on a perturbative propagation of the asymptotic form of ψ_4 at large distances from the sources leading to the following simple expression:

$$\lim_{r \to \infty}[r\psi_4^{\ell m}(r,t)] = \left[r\psi_4^{\ell m}(r,t) - \frac{(\ell-1)(\ell+2)}{2} \right.$$
$$\left. \times \int_0^t dt\, \psi_4^{\ell m}(r,t) \right]_{r=r_{\text{Obs}}} + O(R_{\text{Obs}}^{-2}), \quad (3)$$

where r_{Obs} is the approximate areal radius of the sphere $R_{\text{Obs}} = \text{const}$. [Add a factor $(1/2 - M/r)$ multiplying the square bracket to correct for a difference in normalization between the Psikadelia and Kinnersley tetrads at large distances.] We have found that this formula gives reliable extrapolations for $R_{\text{Obs}} \gtrsim 100M$.

A. Gauge

We obtain accurate, convergent waveforms and horizon parameters by evolving this system in conjunction with a modified $1 + \log$ lapse and a modified Gamma-driver shift condition [5,24], and an initial lapse $\alpha(t=0) = 2/(1 + \psi_{\text{BL}}^4)$. The lapse and shift are evolved with

$$(\partial_t - \beta^i \partial_i)\alpha = -2\alpha K, \quad (4a)$$
$$\partial_t \beta^a = (3/4)\tilde{\Gamma}^a - \eta(x^a, t)\beta^a, \quad (4b)$$

where different functional dependences for $\eta(x^a, t)$ have been proposed in [15,25–29]. Here we use a modification of the form proposed in [25],

$$\eta(x^a, t) = R_0 \frac{\sqrt{\partial_i W \partial_j W \tilde{\gamma}^{ij}}}{(1 - W^a)^b}, \quad (5)$$

where we chose $R_0 = 1.31$. The above gauge condition is inspired by, but differs from Ref. [25] between the BHs and in the outer zones when $a \neq 1$ and $b \neq 2$. Once the conformal factor settles down to its asymptotic $\psi = C/\sqrt{r} + O(1)$ form near the puncture, η will have the form $\eta = (R_0/C^2)(1 + b(r/C^2)^a)$ near the puncture and $\eta = R_0 r^{b-2} M/(aM)^b$ as $r \to \infty$. In practice we used $a = 2$ and $b = 2$, which reduces η by a factor of 4 at infinity when compared to the original version of this gauge proposed by [25]. We note that, if we set $b = 1$, then η will have a $1/r$ falloff at $r = \infty$ as suggested by [26]. Our tests indicate that the choices $(a = 2, b = 1)$ and $(a = 1, b = 1)$ lead to more noise in the waveform than $(a = 2, b = 2)$.

B. Simulations and results

In order to obtain low-eccentricity initial data parameters, we started with quasicircular post-Newtonian initial data parameters for the momenta and particle positions. We then evolved for 1–2 orbits, and used the procedure detailed in [30] to obtain lower eccentricity parameters. In practice we performed between 3 and 4 iterations of the above procedure. In Table I we show the initial data parameters, horizon masses and mass ratio, and initial orbital eccentricities for the three configurations considered here.

In all the simulations presented here, the outer boundaries were placed at $400M$. We performed runs with three resolutions, with a global refinement factor of 1.2 between resolutions. For the $q = 1/10$ runs, we used 11 levels of refinement around the smaller BH, with a central resolution of $h = M/307.2$ for the coarsest runs, while for the $q = 1/15$ run we used 12 levels of refinement, with a central resolution of $M/614.4$. In Table II we show the radiated energy-momentum and remnant BH parameters for these configurations. In the figures and tables below we refer to the different resolution runs using the grid spacing on the coarsest grid relative to $h_0 = 10/3M$.

In Fig. 1 we show the orbital separation as a function of time for the $q10r8.4$ and $q10r7.3$ configurations, as well as a high-eccentricity configuration obtained by directly using PN parameters in the initial data ($q10r7.3$PN) that we

TABLE I.   Initial data parameters. The punctures are located on the x-axis at positions x_1 and x_2, with puncture mass parameters (not horizon masses) m_1 and m_2, and momentum $\pm\vec{p}$. In all cases, the punctures have zero spin. Configuration $q10r7.3$PN is based on the original PN parameters, prior to any eccentricity removal iteration. The lower part of the table shows the horizon masses m_{H_1} and m_{H_2}, the mass ratio q, the ADM mass, and the eccentricity e.

Config	x_1	x_2	p_x	p_y	m_1	m_2
$q10r8.4$	7.633 129	−0.753 175 8	−0.000 168 519	0.036 698 8	0.085 237 27	0.907 396 86
$q10r7.3$	6.604 383	−0.671 518 4	−0.000 219 713	0.041 038 6	0.084 389 51	0.907 038 55
$q10r7.3$PN	6.604 383	−0.671 518 4	−0.000 326 708	0.040 405 7	0.084 389 51	0.907 038 55
$q15r7.3$	6.806 173	−0.443 877 5	−0.000 160 518	0.029 072 1	0.057 566 23	0.936 224 18
Config	m_{H_1}	m_{H_2}	q	M_{ADM}	e	
$q10r8.4$	0.091 289	0.912 545	0.100 04	1.000 042 8	0.0004	
$q10r7.3$	0.091 378	0.913 010	0.100 08	1.000 258 82	0.0017	
$q10r7.3$PN	0.091 329	0.912 990	0.100 03	1.000 000 00	0.008	
$q15r7.3$	0.062 536	0.940 421	0.066 50	1.000 050 83	<0.0015	

TABLE II.   Remnant horizon parameters and radiated energy-momentum.

Config	E_{rad}	J_{rad}	$M_H - M_{ADM}$	$S_{ADM} - S_H$	α	Kick km s^{-1}
$q10r8.4$	$0.004\,46 \pm 0.0001$	0.0517 ± 0.001	$0.000\,46 \pm 0.000\,03$	$0.050\,28 \pm 0.000\,01$	$0.259\,86 \pm 0.000\,01$	59.4 ± 3.0
$q10r7.3$	$0.004\,00 \pm 0.000\,01$	0.0386 ± 0.003	$0.004\,15 \pm 0.000\,01$	$0.040\,28 \pm 0.000\,01$	$0.260\,34 \pm 0.000\,01$	65.8 ± 2.0
$q15r7.3$	$0.002\,16 \pm 0.000\,01$	0.0235 ± 0.0004	$0.002\,25 \pm 0.000\,01$	$0.022\,89 \pm 0.000\,4$	$0.188\,72 \pm 0.000\,01$	33.5 ± 2.1

used for the proof of concept in Ref. [11]. Note that the highly eccentric $q10r7.3$PN binary merges sooner than the lower eccentricity $q10r7.3$. From the plot we can also see that the initial jump in the orbit is not a function of either initial separation or eccentricity. In Fig. 2 we compare the orbital separation for the $q10r7.3$ and $q15r7.3$ configurations. From the plot it is clear that the initial jump in the orbit is not a strong function of mass ratio either. This indicates that the initial jump will become more problematic as the mass ratio is reduced (and hence the inspiral becomes weaker). We also observe that, quite independent of the initial separation and the initial eccentricity, the track displays a universal behavior during the final plunge. This confirms that the tracks are gravitational radiation driven and we are numerically resolving this radiation accurately.

In Fig. 3 we show the orbital trajectories of the $q10r7.3$ and $q15r7.3$ configuration. In the plot the curves have been rotated to maximize the overlap during the plunge. From

the plot we see a "universal" plunge behavior at small separations, with distinctly different orbital dynamics at larger separations. As expected, the small mass ratio binary merges more slowly. In Fig. 4 we show the real part of the ($\ell = 2$, $m = 2$) mode of ψ_4 for the $q10r7.3$ and $q15r7.3$ configurations. Here the we rescaled ψ_4 for $q15r7.3$ by a factor of 1.5. Note that the good overlap of the rescaled ψ_4 indicates that the amplitude of ψ_4 scales with q (before the different orbital dynamics of $q = 1/10$ and $q = 1/15$ cause the $q10r7.3$ to merge sooner). In Fig. 5 we show the convergence of the $q10r7.3$PN configuration for three resolutions. Note that in this plot, the low resolution actually corresponds to a grid spacing 1.2 times larger than the low resolutions for the other configurations. From the plot we can see that at later time the convergence is eighth order. The earlier time fourth-order convergence is due to finite-difference and interpolation errors in the extraction routines. At later times, the phase error dominates the errors in the waveform, and this error converges to eighth order. Finally, in Fig. 6 we show the phase of the waveform for $q15r7.3$ for three resolutions. The phase errors near the plunge are reported in Table III.
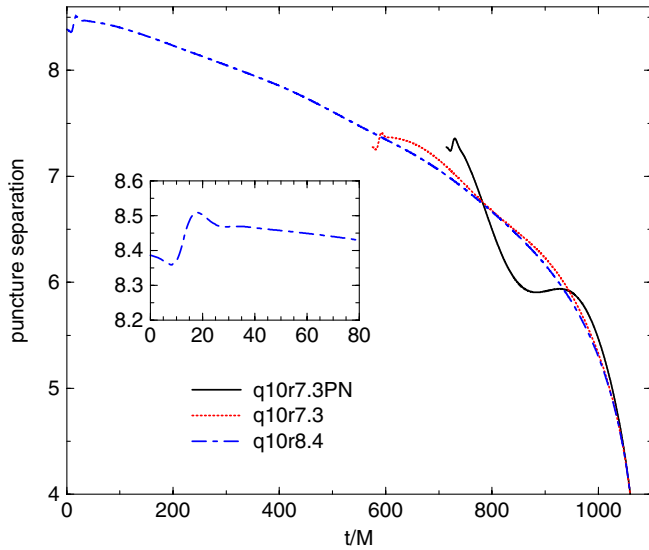

FIG. 1 (color online).   The puncture separation as a function of time for three $q = 1/10$ simulations. The solid curve shows a high-eccentricity simulation obtained from PN quasicircular parameters (with particle limit corrections); the dotted curve shows the results for a binary with the same initial separation after a few iterations to reduce eccentricity; the dot-dashed curve shows an even further separated binary with still smaller eccentricity. Note that the initial jump in the orbit does not appear to be a strong function of the eccentricity or initial separation.
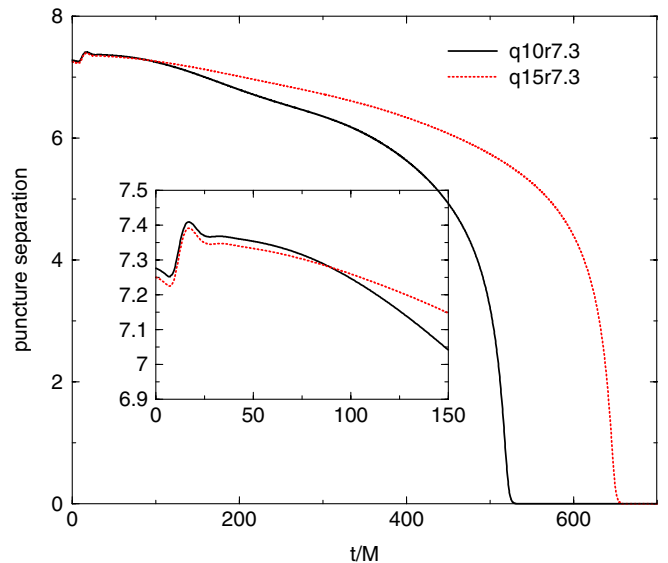

FIG. 2 (color online).   The magnitude of the puncture separation ($|\vec{x}_1 - \vec{x}_2|$) as a function of time for a $q = 1/10$ and $q = 1/15$ binary at similar initial separations. Note that the initial jump in the orbit appears to be independent of q. Also note that the $q = 1/15$ run inspirals more slowly.
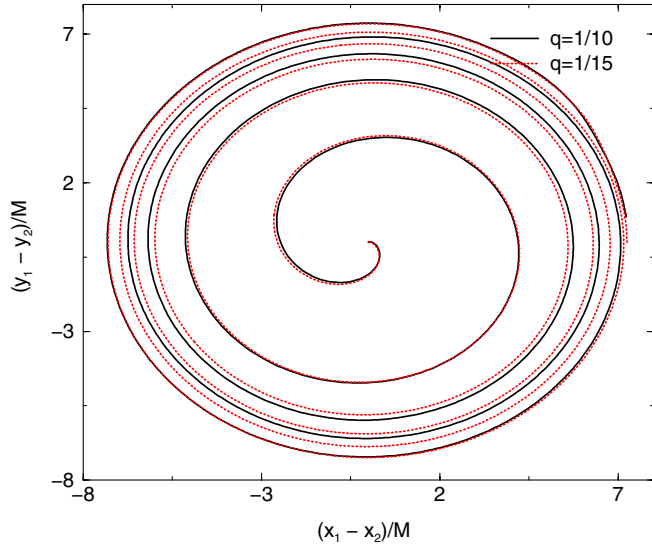
FIG. 3 (color online). An (xy) projection of the puncture separation $(\vec{x}_1 - \vec{x}_2)$ for a $q = 1/10$ and $q = 1/15$ binary at similar initial separations. The trajectories have been rotated so that they overlap during the plunge and merger. Note the "universal" plunge trajectory.
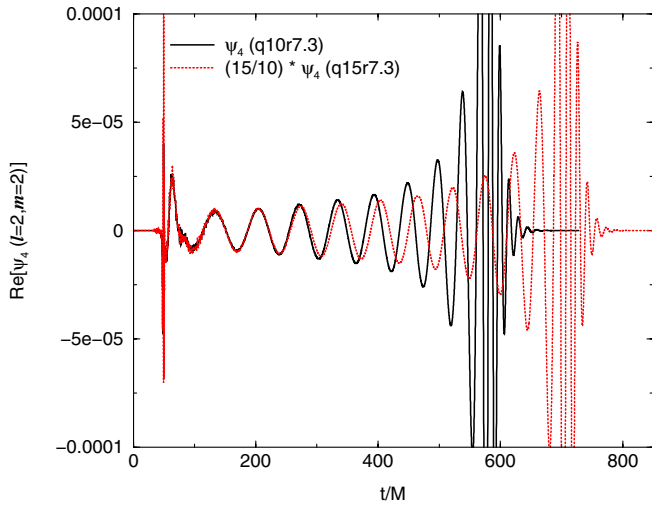

FIG. 4 (color online). The real part of the $(\ell = 2, m = 2)$ mode of ψ_4 for a $q = 1/10$ and $q = 1/15$ binaries starting at similar separations. The waveform from the $q = 1/15$ binary was rescaled by a factor of 1.5 (15/10).

III. PERTURBATIVE TECHNIQUES

In this section we describe in some detail the use of perturbative techniques to produce BHB waveforms from a small mass ratio system. We summarize the key formulae used (for more details see, for instance, [31]), and extend the formalism to add the spin of the large black hole as a second-order perturbation, coupling it to the radiative first-order perturbations. We neglect quadratic terms in the radiative modes of the order $\mathcal{O}(q^2)$. The resulting equations
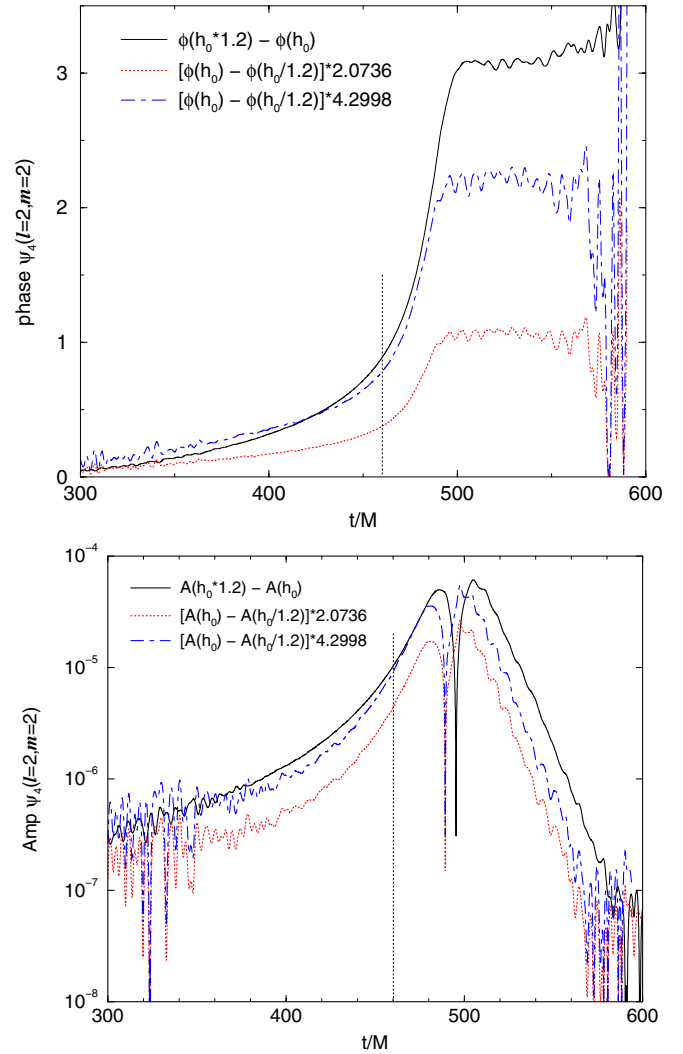
FIG. 5 (color online). The convergence of the phase and amplitude of the $(\ell = 2, m = 2)$ mode of ψ_4 for the $q10r7.3$PN configuration. Note that here the three resolutions consist of a low resolution with grid spacing 1.2 times larger than the low resolution runs for $q10r7.3$, $q10r8.4$, $q15r7.3$ configurations. Eighth-order convergence implies $\psi_4(1.2h_0) - \psi_4(h_0) = 4.29982(\psi_4(h_0) - \psi_4(h_0/1.2))$, while fourth-order convergence implies $\psi_4(1.2h_0) - \psi_4(h_0) = 2.0736(\psi_4(h_0) - \psi_4(h_0/1.2))$. Initially, the error in ψ_4 is very small and dominated by grid noise. Eighth-order convergence in the amplitude is apparent beginning at $t = 320M$, while eighth-order convergence in the phase becomes apparent at $t = 420M$. The dashed vertical line shows the time when the wave frequency is $M\omega = 0.2$. The phase error at this frequency is $\delta\phi \leq 0.2$ rad.

are still of the Regge-Wheeler and Zerilli form (we are still doing perturbations around a Schwarzschild background), but they now include extended source terms with linear dependence on the spin in addition to the local (Dirac's deltas) source terms already present in the first-order formalism. We plug into these latter terms the full numerical trajectories (hence indirectly also adding a spin
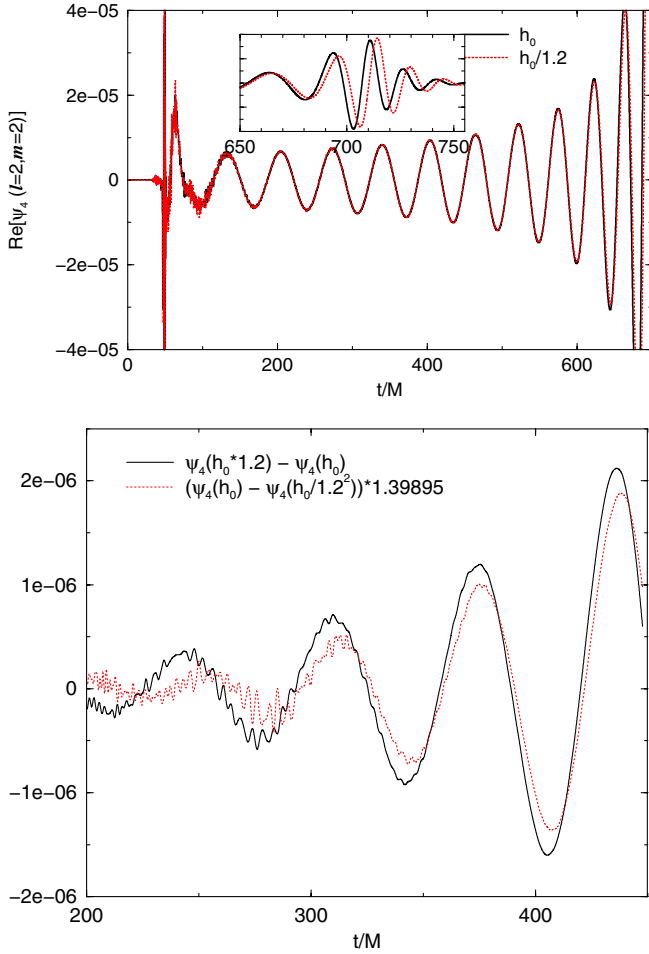
FIG. 6 (color online). (Top) The phase of $(\ell = 2,\ m = 2)$ mode of ψ_4 for a $q = 1/15$ BHB for three resolutions. Note that the phase error only converges to fourth order and that the highest resolution is refined by a factor of 1.2^2 rather than 1.2 with respect to the medium resolution. (Bottom) A convergence plot showing the initial (better than) fourth-order convergence of the waveform. Note here that the differences $\psi_4(1.2h_0) - \psi_4(h_0) = 1.398\,95(\psi_4(h_0) - \psi_4(h_0/1.2^2))$ if the waveform is fourth-order convergent.

TABLE III. The phase error in the $(\ell = 2, m = 2)$ mode of ψ_4 [extracted at $R = 100M$ and extrapolated to ∞ using Eq. (3)] when the waveform frequency is $M\omega = 0.2$ for the medium- and high-resolution runs. The table shows the predicted phase errors extrapolating to infinite resolution and assuming eighth- and fourth-order convergence.

Config	Eighth order	Fourth order
$q10r8.4\ (h = h_0)$	0.205 133	0.630 496
$q10r8.4\ (h = h_0/1.2, \text{pred})$	0.047 707 3	0.304 058
$q10r8.4\ (h = h_0/1.2^2, \text{pred})$	0.011 095 2	0.146 633
$q15r7.25\ (h = h_0/1.2^2)$	0.1406	0.762

dependence). We denote the resulting formalism as spin-Regge-Wheeler-Zerilli (SRWZ).

A. Metric perturbations and particle's orbit

1. Spin as a perturbation

We consider the Kerr metric up to $O(a^1)$. Here a denotes the spin of the black hole which has the dimension of mass. In the usual Boyer-Lindquist coordinates, this is given by

$$ds^2 = -\frac{r - 2M}{r}dt^2 - 4\frac{Ma\sin^2\theta d\phi dt}{r} + \frac{r}{r - 2M}dr^2$$
$$+ r^2 d\theta^2 + r^2\sin^2\theta d\phi^2 + O(a^2). \tag{6}$$

In the above metric, the terms which depend on a are treated as the perturbation in the background Schwarzschild spacetime.

$$g_{\mu\nu} = g^{\text{Sch}}_{\mu\nu} + h^{(1,\text{spin})}_{\mu\nu}. \tag{7}$$

For the above metric perturbations, we consider the tensor harmonics expansion defined using the tensor harmonics of [32]. We find that the first-order perturbation, $O(a^1)$, is related to the $\ell = 1$, $m = 0$ odd parity mode, and the coefficient of the tensor harmonics is given by

$$h^{(1,\text{spin})}_{010}(t, r) = \sqrt{\frac{4\pi}{3}}\frac{2S}{r}, \tag{8}$$

where $S = Ma$. The other components are zero.

2. Second-order formulation

In the following, we treat spin-radiation couplings in the second-order perturbation. Therefore, we consider the Einstein equation in the second perturbative order.

$$G^{(1)}_{\mu\nu}[h^{(1)}] + G^{(1)}_{\mu\nu}[h^{(2)}] + G^{(2)}_{\mu\nu}[h^{(1)}, h^{(1)}]$$
$$= 8\pi(T^{(1)}_{\mu\nu} + T^{(2)}_{\mu\nu}) = 8\pi T_{\mu\nu}, \tag{9}$$

According to [33], and the fact that we use the numerical relativity (NR) trajectory, we do not separate the first- and second-order energy-momentum tensor of the particle. And the second-order metric perturbation, $h^{(2,\text{wave})}$, is created by the spin, $h^{(1,\text{spin})}$-radiation, $h^{(1,\text{wave})}$ couplings. In this case, we may solve

$$G^{(1)}_{\mu\nu}[h^{(1,\text{wave})}] = 8\pi T_{\mu\nu}, \tag{10}$$

$$G^{(1)}_{\mu\nu}[h^{(2,\text{wave})}] = -G^{(2)}_{\mu\nu}[h^{(1,\text{wave})}, h^{(1,\text{spin})}], \tag{11}$$

up to $O(a^1)$, where we ignore the square of the first-order wave functions.

As discussed below, we solve Eqs. (10) and (11) for the even parity perturbation of the Regge-Wheeler-Zerilli formalism in the following form:

$$G^{(1)}_{\mu\nu}[h^{(1,\text{wave})} + h^{(2,\text{wave})}] + G^{(2)}_{\mu\nu}[h^{(1,\text{wave})}, h^{(1,\text{spin})}]$$
$$= G^{(1)}_{\mu\nu}[h^{(\text{wave})}] + G^{(2)}_{\mu\nu}[h^{(\text{wave})}, h^{(1,\text{spin})}] = 8\pi T_{\mu\nu}, \quad (12)$$

where $h^{(\text{wave})} = h^{(1,\text{wave})} + h^{(2,\text{wave})}$. On the other hand, for the odd parity perturbation, Eqs. (10) and (11) are solved for each perturbative order.

Here we consider intermediate mass ratio binaries. As discussed in [34], we can introduce some second-order effects that arise purely from the particle's first-order perturbation, if we treat the particle as a reduced mass $\mu = m_1 m_2/(m_1 + m_2)$ orbiting around a black hole with the total mass $M = m_1 + m_2$.

3. Orbit for inspiral

First, we should note that the coordinates used in NR simulations are chosen to produce stable evolutions and correspond, initially, to isotropic coordinates. Perturbative calculations, on the other hand, regularly make use of the standard Schwarzschild coordinates. The easiest way to relate the two is to translate the numerical tracks into the Schwarzschild coordinates. This can be achieved by considering the late-time numerical coordinates that correspond to radial isotropic "trumpet" stationary $1 + \log$ slices of the Schwarzschild spacetime [35]. We obtain the explicit time and radial coordinate transformations following the procedure detailed in Ref. [36].

Thus, we consider the NR trajectory as an orbit projected on the Schwarzschild background. Therefore, we calculate the particle's energy, angular momentum etc. by using the Schwarzschild metric. Here, since we have only the three velocity $v^i(t)$ from the data of the NR trajectory, the time component of the four velocity u^μ is derived by assuming the "instantaneous" Schwarzschild geodesic approximation.

In this approximation, the energy and angular momentum are given by

$$E = \left(1 - \frac{2M}{R}\right)u^t, \quad (13)$$

$$L_z = R^2 u^\phi, \quad (14)$$

where $u^\mu = dx^\mu/d\tau$ is the four velocity, $R = R(t)$ denotes the orbital radius, and we are considering the equatorial orbit ($\Theta_0 = \pi/2$). To evaluate $U(t) = u^t$, we use

$$g_{\mu\nu}u^\mu u^\nu = -1$$
$$= (U(t))^2 \left[-\left(1 - \frac{2M}{R(t)}\right) + \left(1 - \frac{2M}{R(t)}\right)^{-1}(\dot{R}(t))^2 \right.$$
$$\left. + (R(t))^2(\dot{\Phi}(t))^2 \right]. \quad (15)$$

Here, $\dot{R} = u^r/u^t = dR/dt$ and $\dot{\Phi} = u^\phi/u^t = d\Phi/dt$ are the three velocity of the particle.

We note that the energy E derived from the above $U(t)$ does not decrease monotonically, and also in the end of the orbital evolution, we cannot calculate $U(t)$ appropriately by using Eq. (15), because $U(t) \to \infty$ or becomes complex. $U(t) \to \infty$ is, in practice, not inconsistent because $U(t) \sim (1 - 2M/R(t))^{-1}$ for Schwarzschild geodesics.

Therefore, we fix the energy at some orbital radius (or time $t = t_m$) as

$$E_m = E(t_m) = \left(1 - \frac{2M}{R(t_m)}\right)U(t_m), \quad (16)$$

and use the following expression to obtain $U(t)$ for smaller radii. [This may give the innermost stable circular orbit (ISCO) radius.]

$$U(t) = E_m\left(1 - \frac{2M}{R(t)}\right)^{-1}. \quad (17)$$

At this stage, we still use the three velocity derived from the NR trajectory.

Here we set $R(t_m)/M = 7.64$ for the $q = 1/10$ case. This radius is obtained from the energy minimum evaluated by Eq. (14). In the $q = 1/15$ case, we do not have such an energy minimum. Therefore, we simply set the same radius as for the $q = 1/10$ case.

A. Orbit near merger

There are large differences between the coordinate system used in the NR simulation and the Schwarzschild coordinates near the horizon. Although the binary merges at finite time in the NR simulation, the binary does not merge in the Schwarzschild coordinates. Therefore, we need to give the orbit near the horizon.

Here, we assume that the radiation reaction is not important near merger after $t = t_f$, and use the geodesic orbit on the Schwarzschild spacetime. First, we consider the conserved quantities, i.e., the energy and angular momentum:

$$E_m = E(t_m) = E(t_f),$$
$$L_f = L(t_f) = R(t_f)^2\dot{\Phi}(t_f)E_m\left(1 - \frac{2M}{R(t_f)}\right)^{-1}, \quad (18)$$

where E_m is the same as in the previous section. And then, from the above equations, we calculate

$$U(t) = E_m\left(1 - \frac{2M}{R(t)}\right)^{-1}, \qquad \dot{\Phi}(t) = \frac{L_f}{E_m}\frac{R(t) - 2M}{R(t)^3}. \quad (19)$$

On the other hand, we use a fitting formula for the radial trajectory. By using $g_{\mu\nu}u^\mu u^\nu = -1$, we define an effective energy for the radial motion,

$$E_r^2 = \left(1 - \frac{2M}{R(t_f)}\right)^3 \left(1 + \frac{L_f^2}{R(t_f)^2}\right)\left(\left(1 - \frac{2M}{R(t_f)}\right)^2 - \dot{R}(t_f)^2\right)^{-1},$$

(20)

and consider E_r as a constant after $t = t_f$. The evolution of $\dot{R}(t)$ is derived as

$$\dot{R}(t) = -\left(1 - \frac{2M}{R(t)}\right)\sqrt{1 - \frac{1}{E_r^2}\left(1 - \frac{2M}{R(t)}\right)\left(1 + \frac{L_f^2}{R(t)^2}\right)}.$$

(21)

From this equation, we can obtain various equations if we need, for example, $\ddot{R}(t) = (\partial \dot{R}(t)/\partial R(t))\dot{R}(t)$. It is noted that we may consider another treatment as discussed in Sec. V.

In our perturbative code for both $q = 1/10$ and $1/15$ cases, we set $R(t_f)/M = 3.0$ which is inside the ISCO radius. This is because we want to use the NR trajectories as long as possible in this paper, and the data of the tracks become noisy inside the above orbital radius due to the coordinate transformation.

B. Regge-Wheeler-Zerilli equations with spin

1. First-order Regge-Wheeler-Zerilli equations

For the notation of the Regge-Wheeler-Zerilli formalism [37,38], we use [32,34]. In the first-order perturbation, i.e., the nonspinning case, we may solve the equations,

$$-\frac{\partial^2}{\partial t^2}\Psi_{\ell m}^{(1)}(t, r) + \frac{\partial^2}{\partial r^{*2}}\Psi_{\ell m}^{(1)}(t, r) - V_\ell^{(\text{even})}(r)\Psi_{\ell m}^{(1)}(t, r)$$
$$= S_{\ell m}^{(\text{even},1)}(t, r),$$

(22)

for the even parity with the Zerilli function $\Psi_{\ell m}^{(1)}$, and

$$-\frac{\partial^2}{\partial t^2}\Psi_{\ell m}^{(\text{o},1)}(t, r) + \frac{\partial^2}{\partial r^{*2}}\Psi_{\ell m}^{(\text{o},1)}(t, r) - V_\ell^{(\text{odd})}(r)\Psi_{\ell m}^{(\text{o},1)}(t, r)$$
$$= S_{\ell m}^{(\text{odd},1)}(t, r),$$

(23)

for the odd parity with the Regge-Wheeler function $\Psi_{\ell m}^{(\text{o},1)}$. Here $r^* = r + 2M\ln[r/(2M) - 1]$ is a characteristic coordinate, and the first-order source terms, $S_{\ell m}^{(\text{even},1)}$ and $S_{\ell m}^{(\text{odd},1)}$, are given by

$$S_{\ell m}^{(\text{even},1)}(t, r) = \frac{16\pi(r - 2M)^2(r\ell^2 + r\ell - 4r + 2M)}{\ell(\ell + 1)(r\ell^2 + r\ell - 2r + 6M)r}\mathcal{A}_{\ell m}^{(1)}(t, r) - \frac{16\sqrt{2}\pi(r - 2M)}{\sqrt{\ell(\ell + 1)(\ell - 1)(\ell + 2)}}\mathcal{F}_{\ell m}^{(1)}(t, r)$$

$$+ \frac{32\pi(r - 2M)^2\sqrt{2}}{(r\ell^2 + r\ell - 2r + 6M)\sqrt{\ell(\ell + 1)}}\mathcal{B}_{\ell m}^{(1)}(t, r) - \frac{32\pi(r - 2M)^3}{(r\ell^2 + r\ell - 2r + 6M)\ell(\ell + 1)}\frac{\partial}{\partial r}\mathcal{A}_{\ell m}^{(1)}(t, r)$$

$$- \frac{16\pi r(\ell^4 r^2 + 2r^2\ell^3 - 5r^2\ell^2 + 16r\ell^2 M - 6r^2\ell + 16r\ell M + 8r^2 - 68rM + 108M^2)}{(\ell + 1)\ell(r\ell^2 + r\ell - 2r + 6M)^2}\mathcal{A}_{0\ell m}^{(1)}(t, r)$$

$$+ \frac{32\pi(r - 2M)r^2}{(r\ell^2 + r\ell - 2r + 6M)\ell(\ell + 1)}\frac{\partial}{\partial r}\mathcal{A}_{0\ell m}^{(1)}(t, r) + \frac{32\sqrt{2}\pi(r - 2M)^2}{(r\ell^2 + r\ell - 2r + 6M)\ell(\ell + 1)}\mathcal{G}_{\ell m}^{(1)}(t, r),$$

$$S_{\ell m}^{(\text{odd},1)}(t, r) = \frac{16\sqrt{2}\pi(r - 2M)}{\sqrt{\ell(\ell + 1)(\ell - 1)(\ell + 2)}}\mathcal{Q}_{0\ell m}^{(1)}(t, r) + \frac{16\sqrt{2}\pi r(r - 2M)}{\sqrt{\ell(\ell + 1)(\ell - 1)(\ell + 2)}}\frac{\partial}{\partial r}\mathcal{Q}_{0\ell m}^{(1)}(t, r)$$

$$- \frac{16\sqrt{2}i\pi r(r - 2M)}{\sqrt{\ell(\ell + 1)(\ell - 1)(\ell + 2)}}\frac{\partial}{\partial t}\mathcal{Q}_{\ell m}^{(1)}(t, r),$$

(24)

where $\mathcal{A}_{\ell m}^{(1)}$ etc. denote the tensor harmonics coefficient of the particle's energy-momentum tensor $T_{\mu\nu}$. It is noted that the even parity wave function $\Psi_{\ell m}^{(1)}$ and odd parity wave function $\Psi_{\ell m}^{(\text{o},1)}$ are related to the Moncrief's [39] and the Cunningham *et al.* [40] waveforms by a normalization factor, respectively.

2. Even parity perturbation with spin

When we discuss only the second-order Einstein equation in Eq. (11) for the even parity perturbation, the Zerilli equation with the $O(a^1)$ spin effect is written as

$$-\frac{\partial^2}{\partial t^2}\Psi_{\ell m}^{(2)}(t, r) + \frac{\partial^2}{\partial r^{*2}}\Psi_{\ell m}^{(2)}(t, r) - V_\ell^{(\text{even})}(r)\Psi_{\ell m}^{(2)}(t, r) = S_{\ell m}^{(\text{even},2)}(t, r),$$

(25)

where the second-order source term $S_{\ell m}^{(\text{even},2)}$ in the above equation is given by

$$S_{\ell m}^{(even,2)}(t,r) = S_{\ell m}^{(even,2)}(E,S) + S_{\ell m}^{(even,2)}(O,S);$$

$$S_{\ell m}^{(even,2)}(E,S) = \frac{mS}{\ell(\ell+1)(r\ell^2+r\ell-2r+6M)}\left(64\frac{\sqrt{2}\pi(-r+2M)(-2r+r\ell+r\ell^2+12M)}{\sqrt{\ell(\ell+1)}r(r\ell^2+r\ell-2r+6M)}\mathcal{B}_{0\ell m}^{(1)}(t,r)\right.$$

$$+64\frac{\sqrt{2}\pi(-r+2M)}{r}\mathcal{A}_{1\ell m}^{(1)}(t,r) + \frac{192i(-r+2M)\pi\sqrt{2}}{\sqrt{\ell(\ell+1)(\ell-1)(\ell+2)}}\partial_t\mathcal{F}_{\ell m}^{(1)}(t,r)$$

$$+\frac{8i(12M-6r+\ell^4 r+2r\ell^3+r\ell+2r\ell^2)(-r+2M)}{r^3(r\ell^2+r\ell-2r+6M)}H_{1\ell m}^{(1)}(t,r) + \frac{8i\ell(\ell+1)}{r}\partial_t K_{\ell m}^{(1)}(t,r)\Bigg),$$

$$S_{\ell m}^{(even,2)}(O,S) = \frac{4S}{\ell(\ell+1)(\ell-1)(\ell+2)}\sqrt{\frac{(\ell-m)(\ell+m)}{(2\ell-1)(2\ell+1)}}\Bigg(6(r-2M)(2\ell^4 r^2 - 4r^2\ell^2 + 6r^2 + r^2\ell^5 - 5r^2\ell$$

$$-28rM + 12r\ell M + 4\ell^3 rM + 12r\ell^2 M + 36M^2)(\ell-1)(\ell+2)/[(r\ell^2+r\ell-2r+6M)^2 r^5]$$

$$\times(r\partial_t h_{1\ell-1m}^{(1)}(t,r) + 2h_{0\ell-1m}^{(1)}(t,r) - r\partial_r h_{0\ell-1m}^{(1)}(t,r))$$

$$+32\frac{\sqrt{2}\pi(\ell+2)(r\ell^2+r\ell-2r+3M)(\ell-1)^2(r-2M)}{r\sqrt{(\ell-1)\ell}(r\ell^2+r\ell-2r+6M)^2}Q_{0\ell-1m}^{(1)}(t,r)\Bigg)$$

$$+\frac{4S}{\ell(\ell+1)(\ell-1)(\ell+2)}\sqrt{\frac{(\ell+m+1)(\ell-m+1)}{(2\ell+1)(2\ell+3)}}\Bigg(-6(r-2M)(2r^2\ell^2 + 32rM - 36M^2 + 3\ell^4 r^2$$

$$+4\ell^3 rM + r^2\ell^5 + 2r^2\ell^3 - 8r^2)(\ell-1)(\ell+2)/[(r\ell^2+r\ell-2r+6M)^2 r^5]$$

$$\times(r\partial_t h_{1\ell+1m}^{(1)}(t,r)r + 2h_{0\ell+1m}^{(1)}(t,r) - r\partial_r h_{0\ell+1m}^{(1)}(t,r))$$

$$-32\frac{\sqrt{2}\pi(\ell-1)(r\ell^2+r\ell-2r+3M)(\ell+2)^2(r-2M)}{r\sqrt{(\ell+1)(\ell+2)}(r\ell^2+r\ell-2r+6M)^2}Q_{0\ell+1m}^{(1)}(t,r)\Bigg). \tag{26}$$

In Eq. (26), $S_{\ell m}^{(even,2)}(E,S)$ and $S_{\ell m}^{(even,2)}(O,S)$ mean the coupling between the black hole's spin and the first-order even and odd parity perturbations, respectively. The tensor harmonics coefficients of the first-order metric perturbation, $H_{1\ell m}^{(1)}$ etc. are written in terms of the first-order Regge-Wheeler and Zerilli functions.

Here, we introduce the following combined function:

$$\Psi_{\ell m}(t,r) = \Psi_{\ell m}^{(1)}(t,r) + \Psi_{\ell m}^{(2)}(t,r), \tag{27}$$

which is the linear combination of the first- and second-order wave functions. This function formally satisfies

$$-\frac{\partial^2}{\partial t^2}\Psi_{\ell m}(t,r) + \frac{\partial^2}{\partial r^{*2}}\Psi_{\ell m}(t,r) - V_\ell^{(even)}(r)\Psi_{\ell m}(t,r) + iSmP_\ell^{(even,1)}(r)\frac{\partial}{\partial t}\Psi_{\ell m}(t,r) + iSmP_\ell^{(even,2)}(r)\frac{\partial^2}{\partial t\partial r}\Psi_{\ell m}(t,r)$$

$$= S\sqrt{\frac{(\ell-m)(\ell+m)}{(2\ell-1)(2\ell+1)}}Q_\ell^{(even,-)}(r)\Psi_{\ell-1m}^{(o,1)}(t,r) + S\sqrt{\frac{(\ell+m+1)(\ell-m+1)}{(2\ell+1)(2\ell+3)}}Q_\ell^{(even,+)}(r)\Psi_{\ell+1m}^{(o,1)}(t,r) + S_{\ell m}^{(even,L)}(t,r), \tag{28}$$

where $S_{\ell m}^{(even,L)}(t,r)$ denotes the local source term with the Dirac's delta function and its derivative. The explicit expression and some detailed analysis are given in Appendix A 1.

3. Odd parity perturbation with spin

In the first perturbative order calculation, we have used the Cunningham *et al.* waveform $\Psi_{\ell m}^{(o,1)}$ for the odd parity as the Regge-Wheeler function. When we use $\Psi_{\ell m}^{(o,2)}$, we have some trouble in the source terms of the perturbed Regge-Wheeler (odd parity) equation. The second-order local source term does not vanish at the horizon. Therefore,

we use the Zerilli waveform $\Psi_{\ell m}^{(o,Z,2)}$ instead of the Cunningham *et al.* waveform $\Psi_{\ell m}^{(o,2)}$ in the second perturbative order

$$-\frac{\partial^2}{\partial t^2}\Psi_{\ell m}^{(o,Z,2)}(t,r) + \frac{\partial^2}{\partial r^{*2}}\Psi_{\ell m}^{(o,Z,2)}(t,r)$$

$$- V_\ell^{(odd)}(r)\Psi_{\ell m}^{(o,Z,2)}(t,r) = S_{\ell m}^{(odd,Z,2)}(t,r), \tag{29}$$

where the second-order source term $S_{\ell m}^{(odd,Z,2)}$ is formally given as

$$S_{\ell m}^{(\text{odd},Z,2)}(t, r) = \frac{8\sqrt{2}\pi i(r - 2M)^2}{r^2\sqrt{\ell(\ell+1)}} \mathcal{Q}_{\ell m}^{(2)}(t, r)$$

$$- \frac{16\sqrt{2}\pi i M(r - 2M)}{r^2\sqrt{\ell(\ell+1)(\ell-1)(\ell+2)}} \mathcal{D}_{\ell m}^{(2)}(t, r)$$

$$- \frac{8\sqrt{2}\pi i(r - 2M)^2}{r\sqrt{\ell(\ell+1)(\ell-1)(\ell+2)}} \frac{\partial}{\partial r} \mathcal{D}_{\ell m}^{(2)}(t, r).$$

$$(30)$$

$\mathcal{Q}_{\ell m}^{(2)}$ and $\mathcal{D}_{\ell m}^{(2)}$ are calculated by the tensor harmonics expansion of $-G_{\mu\nu}^{(2)}[h^{(1,\text{wave})}, h^{(1,\text{spin})}]/(8\pi)$ from the second-order Einstein tensor. And using $\mathcal{Q}_{\ell m}^{(2)}$, we have the relation between the two waveforms $\Psi_{\ell m}^{(o,2)}$ and $\Psi_{\ell m}^{(o,Z,2)}$ as

$$\partial_t \Psi_{\ell m}^{(o,2)}(t, r)$$

$$= 2\Psi_{\ell m}^{(o,Z,2)}(t, r) + \frac{16\sqrt{2}\pi i r(r - 2M)}{(\ell-1)(\ell+2)\sqrt{\ell(\ell+1)}} \mathcal{Q}_{\ell m}^{(2)}(t, r).$$

$$(31)$$

For the wave equation of $\Psi_{\ell m}^{(o,Z,2)}$, we have the second-order source term as

$$S_{\ell m}^{(\text{odd},Z,2)}(t, r) = S_{\ell m}^{(\text{odd},Z,2)}(E, S) + S_{\ell m}^{(\text{odd},Z,2)}(O, S);$$

$$S_{\ell m}^{(\text{odd},Z,2)}(E, S) = \frac{4S}{\ell(\ell+1)(\ell-1)(\ell+2)}\sqrt{\frac{(\ell-m)(\ell+m)}{(2\ell-1)(2\ell+1)}}\left(3\frac{(r-2M)(\ell-1)(\ell+2)(\ell+1)}{r^4}\partial_t K_{\ell-1m}^{(1)}(t, r)\right.$$

$$\left.+ 12\frac{\sqrt{2}\pi(r-2M)(\ell-1)(\ell+2)(\ell+1)}{r^2\sqrt{(\ell-1)\ell(\ell-2)(\ell+1)}}\partial_t \mathcal{F}_{\ell-1m}^{(1)}(t, r)\right) + \frac{4S}{\ell(\ell+1)(\ell-1)(\ell+2)}$$

$$\times\sqrt{\frac{(\ell+m+1)(\ell-m+1)}{(2\ell+1)(2\ell+3)}}\left(-3\frac{(r-2M)\ell(\ell-1)(\ell+2)}{r^4}\partial_t K_{\ell+1m}^{(1)}(t, r)\right.$$

$$\left.- 12\frac{\sqrt{2}\pi(r-2M)\ell(\ell-1)(\ell+2)}{r^2\sqrt{(\ell+1)(\ell+2)\ell(\ell+3)}}\partial_t \mathcal{F}_{\ell+1m}^{(1)}(t, r)\right),$$

$$S_{\ell m}^{(\text{odd},Z,2)}(O, S) = \frac{Sm}{\ell(\ell+1)}\left(\frac{-48\sqrt{2}i\pi(r-2M)}{\sqrt{\ell(\ell+1)}r^3}\mathcal{Q}_{0\ell m}^{(1)}(t, r) - \frac{12i(6r+r\ell+r\ell^2-14M)(r-2M)}{r^7}h_{0\ell m}^{(1)}(t, r)\right.$$

$$\left.+ \frac{12i(r-2M)(3r-7M)}{r^6}\partial_r h_{0\ell m}^{(1)}(t, r) + \frac{4i(-9r+r\ell+r\ell^2+21M)(r-2M)}{r^6}\partial_t h_{1\ell m}^{(1)}(t, r)\right), \quad (32)$$

without any regularization (or modification) of the wave function. Here, we note that $S_{\ell m}^{(\text{odd},Z,2)}(E, S)$ for the $\ell = 3$, $m = 2$ mode is the time derivative of the second-order term in Eq. (76) of [41]. The explicit expression of Eq. (29) is given in Appendix A 2. We should note that for the $\ell = 2$ mode, there is an ill-defined term due to the factor $(\ell - 2)$ in the denominator. This is why we need a special treatment for the $\ell = 1$ mode in the next section.

4. For lower ℓ modes

In the calculation of the second-order $\ell = 2$ odd parity perturbation, we have the first-order $\ell = 1$ mode contribution. In [38], this $\ell = 1$ mode has been calculated under the Zerilli gauge, i.e., $K_{1m} = h_{01m}^{(e)} = h_{11m}^{(e)} = 0$.

$$H_{01m}^{(1)Z}(t, r) = \frac{1}{3M(r-2M)^2}\left(r^3\frac{d^2}{dt^2}f_m(t) + Mf_m(t)\right)\theta(r - R(t)),$$

$$H_{11m}^{(1)Z}(t, r) = -\frac{r}{(r-2M)^2}\frac{d}{dt}f_m(t)\theta(r - R(t)),$$

$$H_{21m}^{(1)Z}(t, r) = \frac{1}{(r-2M)^2}f_m(t)\theta(r - R(t)),$$

$$(33)$$

where

$$f_m(t) = 8\pi\mu U(t)\frac{(R(t) - 2M)^2}{R(t)}Y_{1m}^*(\Theta_0, \Phi(t)). \quad (34)$$

Here $*$ denotes the complex conjugate. There is no contribution from the $m = 0$ mode.

Using the above first-order $\ell = 1$ mode, we calculate the second-order source term from the coupling between this mode and the black hole's spin. Then the source term becomes finite at the horizon. In order to remove this finite term, we introduce a regularization function,

$$\Psi_{2m}^{(o,Z,2)}(t, r) = \Psi_{2m}^{(o,Z,2),R}(t, r) - \frac{S\sqrt{15(2 - m)(2 + m)}}{30Mr(r - 2M)} \dot{f}_m(t)\theta(r - R(t)), \tag{35}$$

and we solve the wave equation for the regularized function $\Psi_{2m}^{(o,Z,2),R}$. Here, we note that the regularization function does not affect the waveform at infinity in our calculation. The regularized second-order source term is derived as

$$
\begin{aligned}
S_{2m}^{(odd,Z,2),R}(E, S, [\ell = 1]) = {} & \frac{4\sqrt{15}\pi\mu S\sqrt{(2 - m)(2 + m)}}{15} Y_{1m}^*(\Theta_0, \Phi(t))\Bigg[\Bigg(\frac{im(R(t) - 2M)^2 U(t)(\dot{\Phi}(t))^3}{R(t)M} \\
& + \frac{\dot{R}(t)U(t)(R(t) - 2M)(\dot{\Phi}(t))^2}{R(t)M} - \frac{im(R(t) - 2M)^2\dot{\Phi}(t)}{(R(t))^3 MU(t)} + \frac{\dot{R}(t)(R(t) - 2M)}{(R(t))^3 MU(t)}\Bigg)\frac{d}{dr}\delta(r - R(t)) \\
& + \Bigg(\frac{im(R(t) - 2M)(13M - 3R(t))(\dot{\Phi}(t))^3 U(t)}{(R(t))^2 M} - \frac{2im(5M - 2R(t))(R(t) - 2M)^2\dot{\Phi}(t)U(t)}{(R(t))^5 M} \\
& - 4\frac{(R(t) - 2M)^2\dot{R}(t)U(t)}{(R(t))^5 M} + \frac{(-12M + 2Mm^2 - m^2R(t) + 4R(t))(\dot{\Phi}(t))^2\dot{R}(t)U(t)}{(R(t))^2 M} \\
& + \frac{im(11M - 2R(t))(R(t) - 2M)\dot{\Phi}(t)}{(R(t))^4 MU(t)} - 2\frac{(4M - R(t))\dot{R}(t)}{(R(t))^4 MU(t)}\Bigg)\delta(r - R(t))\Bigg]. \tag{36}
\end{aligned}
$$

We have only the local source contributions as the second-order source term from this mode. Using the following asymptotic behavior near the horizon, $U(t) \sim (1 - 2M/R(t))^{-1}$, $\dot{R}(t) \sim (1 - 2M/R(t))$, and $\dot{\Phi}(t) \sim (1 - 2M/R(t))$, we find that the above source term vanishes at the horizon in the integration of the wave equation.

5. Symmetry in $\Psi_{\ell m}$ and $\Psi_{\ell m}^{(o)}$

In this subsection, we use the notation $\Psi_{\ell m}^{(even)} = \Psi_{\ell m}$ and $\Psi_{\ell m}^{(odd)} = \Psi_{\ell m}^{(o)}$, which have the following relation in the first perturbative order:

$$\Psi_{\ell-m}^{(even/odd)} = (-1)^m(\Psi_{\ell m}^{(even/odd)})^*. \tag{37}$$

This is derived from a formula for the spherical harmonics,

$$Y_{\ell-m}(\theta, \phi) = (-1)^m Y_{\ell m}^*(\theta, \phi). \tag{38}$$

In the $O(a^1)$ calculation, we should have the same symmetry because the metric perturbations become real. We can check this by using the explicit form of $S_{\ell m}^{(even/odd)}$.

6. Gravitational waves

In the above sections, we discussed the techniques to calculate the wave functions $\Psi_{\ell m} = \Psi_{\ell m}^{(1)} + \Psi_{\ell m}^{(2)}$, $\Psi_{\ell m}^{(o,1)}$, and $\Psi_{\ell m}^{(o,Z,2)}$. The first-order wave functions and waveforms at infinity are simply related as

$$
\begin{aligned}
h_+ - ih_\times = {} & \sum \frac{\sqrt{(\ell - 1)\ell(\ell + 1)(\ell + 2)}}{2r} \\
& \times (\Psi_{\ell m}^{(1)} - i\Psi_{\ell m}^{(o,1)})_{-2}Y_{\ell m}, \tag{39}
\end{aligned}
$$

where $_{-2}Y_{\ell m}$ denotes the spin-weighted spherical harmonics used in [42].

On the other hand, in order to discuss gravitational waveforms in the second perturbative order, we need to check the asymptotic behavior of the metric perturbation and the contributions from the first-order gauge transformation. First, we evaluate the asymptotic behavior of the tensor harmonics coefficients of $G_{\mu\nu}^{(2)}$, because this information is used to construct the metric perturbation from the wave functions. For the odd parity-spin coupling part, we have the following behavior:

$$
\begin{aligned}
& \mathcal{A}_{0\ell m}^{(2)}(O, S) \sim O(1/r^3), \quad \mathcal{A}_{1\ell m}^{(2)}(O, S) \sim O(1/r^3), \\
& \mathcal{A}_{\ell m}^{(2)}(O, S) \sim O(1/r^3), \quad \mathcal{B}_{0\ell m}^{(2)}(O, S) \sim O(1/r^3), \\
& \mathcal{B}_{\ell m}^{(2)}(O, S) \sim O(1/r^3), \quad \mathcal{G}_{\ell m}^{(2)}(O, S) \sim O(1/r^3), \\
& \mathcal{F}_{\ell m}^{(2)}(O, S) \sim O(1/r^4), \quad \mathcal{Q}_{\ell m}^{(2)}(O, S) \sim O(1/r^3), \\
& \mathcal{Q}_{1\ell m}^{(2)}(O, S) \sim O(1/r^3), \quad \mathcal{D}_{\ell m}^{(2)}(O, S) \sim O(1/r^4),
\end{aligned} \tag{40}
$$

and for the even parity-spin coupling part,

$$
\begin{aligned}
& \mathcal{A}_{0\ell m}^{(2)}(E, S) \sim O(1/r^3), \quad \mathcal{A}_{1\ell m}^{(2)}(E, S) \sim O(1/r^3), \\
& \mathcal{A}_{\ell m}^{(2)}(E, S) \sim O(1/r^3), \quad \mathcal{B}_{0\ell m}^{(2)}(E, S) \sim O(1/r^2), \\
& \mathcal{B}_{\ell m}^{(2)}(E, S) \sim O(1/r^2), \quad \mathcal{G}_{\ell m}^{(2)}(E, S) \sim O(1/r^4), \\
& \mathcal{F}_{\ell m}^{(2)}(E, S) \sim O(1/r^3), \quad \mathcal{Q}_{\ell m}^{(2)}(E, S) \sim O(1/r^2), \\
& \mathcal{Q}_{1\ell m}^{(2)}(E, S) \sim O(1/r^2), \quad \mathcal{D}_{\ell m}^{(2)}(E, S) \sim O(1/r^3).
\end{aligned} \tag{41}
$$

And the even parity-spin coupling part from the $\ell = 1$ even parity has a different behavior:

$$Q_{2m}^{(2)}(E, S, [\ell = 1]) \sim O(1/r^3),$$
$$Q_{12m}^{(2)}(E, S, [\ell = 1]) \sim O(1/r^2), \tag{42}$$

and $\mathcal{D}_{2m}^{(2)}(E, S, [\ell = 1]) = 0$ in the first-order Zerilli gauge.

From the above asymptotic behaviors, if we set the observer location to a large distance, we do not need to consider these tensor harmonics contributions because the contributions are at least $O(1/r)$ lower than the leading part. Note that the metric reconstruction in the second-order odd parity perturbation has been done from the Zerilli waveform $\Psi_{\ell m}^{(o,Z,2)}$.

Next, we discuss the contributions from the first-order gauge transformation. Formally the following gauge transformation [43] is used in the second-order calculation:

$$x_{RW}^\mu \rightarrow x_{AF}^\mu = x_{RW}^\mu + \xi^{(1)\mu}(x^\alpha)$$
$$+ \frac{1}{2}[\xi^{(2)\mu}(x^\alpha) + \xi^{(1)\nu}\xi_{,\nu}^{(1)\mu}(x^\alpha)], \tag{43}$$

where comma "," in the index indicates the partial derivative with respect to the background Schwarzschild coordinates, and $\xi^{(1)\mu}$ and $\xi^{(2)\mu}$ are generators of the first- and second-order gauge transformations, respectively. The subscripts RW and AF show the Regge-Wheeler gauge where we reconstruct the metric perturbation, and the asymptotic flat gauge where we obtain the gravitational waveforms, respectively. Then, the metric perturbations change to

$$h_{RW\mu\nu}^{(1)} \rightarrow h_{AF\mu\nu}^{(1)} = h_{RW\mu\nu}^{(1)} - \mathcal{L}_{\xi^{(1)}}g_{\mu\nu}, \tag{44}$$

$$h_{RW\mu\nu}^{(2)} \rightarrow h_{AF\mu\nu}^{(2)} = h_{RW\mu\nu}^{(2)} - \frac{1}{2}\mathcal{L}_{\xi^{(2)}}g_{\mu\nu}$$
$$+ \frac{1}{2}\mathcal{L}_{\xi^{(1)}}^2 g_{\mu\nu} - \mathcal{L}_{\xi^{(1)}}h_{RW\mu\nu}^{(1)}, \tag{45}$$

where $\mathcal{L}_{\xi^{(i)}}$ denotes the Lie derivative.

In this paper, second perturbative order means $O(\mu a)$ where μ and a are small quantities. Since $\xi^{(1)}$ is $O(\mu)$, we ignore $\mathcal{L}_{\xi^{(1)}}^2 g_{\mu\nu}$ and $\mathcal{L}_{\xi^{(1)}}h_{RW\mu\nu}^{(1)}$ with $h_{RW\mu\nu}^{(1)} \sim O(\mu)$ in Eq. (45). On the other hand, there is a contribution from $\mathcal{L}_{\xi^{(1)}}h_{\mu\nu}^{(1,\text{spin})}$. The asymptotic behavior of this tensor harmonics coefficient becomes

$$\delta H_{0\ell m} \sim O(1/r), \qquad \delta H_{1\ell m} \sim O(1/r),$$
$$\delta H_{2\ell m} = 0, \qquad \delta h_{0\ell m}^{(e)} \sim O(r^0),$$
$$\delta h_{1\ell m}^{(e)} \sim O(r^0), \qquad \delta G_{\ell m} \sim O(1/r^2),$$
$$\delta K_{\ell m} \sim O(1/r^2), \qquad \delta h_{0\ell m} \sim O(r^0),$$
$$\delta h_{1\ell m} \sim O(r^0), \qquad \delta h_{2\ell m} \sim O(r^0). \tag{46}$$

For the $\ell = 1$ mode in the first perturbative order when we consider the gauge transformation to the center of mass coordinates, we have the same behaviors. These contributions to the second-order metric perturbation under the

Regge-Wheeler gauge are also lower order by $O(1/r)$ at least.

Finally, to derive the waveforms in the SRWZ formalism, we may consider

$$h_+ - ih_\times = \sum \frac{\sqrt{(\ell - 1)\ell(\ell + 1)(\ell + 2)}}{2r}$$
$$\times (\Psi_{\ell m} - i\Psi_{\ell m}^{(o)})_{-2}Y_{\ell m}, \tag{47}$$

where again $\Psi_{\ell m} = \Psi_{\ell m}^{(1)} + \Psi_{\ell m}^{(2)}$. Note that for $\Psi_{\ell m}^{(o)}$ we have used a different wave functions for the first- and second-order odd parity calculations for the sake of simplicity of the final results. Using Eq. (31) and the above asymptotic behaviors of $Q_{\ell m}^{(2)}$, we simply combine them as

$$\Psi_{\ell m}^{(o)} = \Psi_{\ell m}^{(o,1)} + 2\int dt \Psi_{\ell m}^{(o,Z,2)}. \tag{48}$$

7. Observer location effect

In [11], we saw that the observer location effect was not negligible on the waveforms. To compare the NR and perturbative waveforms, we directly use Eq. (47) because we can set the extraction radius of gravitational waves at a sufficiently distant location, for example, $R_{\text{Obs}}/M = 1000$. On the other hand, the NR waveforms are obtained from the NR ψ_4 data

$$\psi_4 = \ddot{h}_+ - i\ddot{h}_\times. \tag{49}$$

We should note that these are true only at $R_{\text{Obs}} \rightarrow \infty$.

First, we discuss the asymptotic behavior of the (first-order) Regge-Wheeler-Zerilli functions. In general ℓ modes for both the even and odd parities, which we denote by $\Psi_{\ell m}^{(\text{even})}$ and $\Psi_{\ell m}^{(\text{odd})}$, are given by

$$\Psi_{\ell m}^{(\text{even/odd})} = H_{\ell m}(t - r^*) + \frac{\ell(\ell + 1)}{2r}\int dt H_{\ell m}(t - r^*)$$
$$+ O(r^{-2}). \tag{50}$$

We note that errors due to finite extraction radii, which arise from the integral term in Eq.(50), are larger for lower frequencies due to the $1/\omega$ obtained by integrating a function with a frequency ω.

Next, we discuss the relation between Regge-Wheeler-Zerilli functions and the mode function $\psi_4^{\ell m}$ of the Weyl scalar. Here, although we can use the formula given in Eqs. (C.1) and (C.2) of [44], we use simpler formulae valid for the asymptotic behavior of the functions. If the NR Weyl scalar satisfies the Teukolsky equation in the Schwarzschild spacetime, we have

$$r\psi_4^{\ell m} = \ddot{\ddot{H}}_{\ell m}(t - r^*) + \frac{(\ell - 1)(\ell + 2)}{2r}\dot{H}_{\ell m}(t - r^*)$$
$$+ O(r^{-2}), \tag{51}$$

where the difference between $\tilde{H}_{\ell m}$ and $H_{\ell m}$ in Eq. (50) is only the numerical factor.

Combining the above equation with Eq. (50), we have

$$r\psi_4^{\ell m} \sim \ddot{\tilde{\Psi}}_{\ell m}^{(even/odd)} - \frac{1}{r}\int dt\, \ddot{\tilde{\Psi}}_{\ell m}^{(even/odd)} + O(r^{-2}), \quad (52)$$

which is independent of ℓ and parity modes. This equation is consistent with the formula in [44]. Here, we have considered the correction for the RWZ functions. It is important, however, to calculate $H_{\ell m}$, the waveform at infinity, because the PN waveforms, which are used to construct the hybrid waveform, do not have the finite observer location effects.

Therefore, we consider the extrapolation of the NR ψ_4 from, for example, $R_{Obs}/M = 100$ to infinity by using Eq. (51):

$$\ddot{\tilde{H}}_{\ell m} = R_{Obs}\psi_4^{\ell m} - \frac{(\ell - 1)(\ell + 2)}{2}\int dt\,\psi_4^{\ell m} + O(R_{Obs}^{-2}).$$

$$(53)$$

Again, the above formula is derived by assuming the Teukolsky equation in the Schwarzschild spacetime ($a = 0$). Since we treat only the extrapolation from $R_{Obs}/M = 100$ to infinity, we may use the wave (linear propagation) equation in the flat spacetime. Thus, the Teukolsky equation with $M \to 0$ is sufficient to discuss the extrapolation. This calculation gives the same result as Eq. (53). Note that since the above formulation has been discussed by using the Weyl scalar in the Kinnersley tetrad, we need an extra factor as the explanation below Eq. (3) for that in another tetrad.

Let us point out that full numerical methods using Cauchy-characteristic methods have been developed [45]. Also multipatch [46] and pseudospectral [10] techniques allow extraction radii very far from the source.

8. Numerical integration method

Although we have used the combination of Eq. (27) for the even parity perturbation and integrate Eq. (28) in this paper, the basic equations are the four wave equations, (22) and (23) for the first perturbative order and (25) and (29) for the second perturbative order.

In order to integrate the resulting even and odd parity wave equations, we use the method described in [47]. This method is second-order accurate in the grid spacing (see [31] for a fourth-order formalism), but deals with the Dirac's delta source "exactly" or as accurately as needed.

Even if we considered the metric (6) with first-order spin corrections to the Schwarzschild metric, the method of perturbations we used still propagates waves on the exact Schwarzschild background and lumps the spin corrections in a source term, as if they would be second-order perturbations. We hence apply the methods of [31,47] with an added smooth source to integrate the first order in spin-corrected RWZ wave equations. We proved second-order convergence of the extracted waveforms and used spatial

and time steps that produced errors well below those acceptable for full numerical evolutions. The runs typically take under a minute on a laptop and are very low in memory and resources requirements. We also note that these types of codes are amenable to implementation on accelerated hardware such as GPUs or cell processors [48].

IV. ANALYSIS OF THE NUMERICAL VERSUS PERTURBATIVE RESULTS

Here we directly compare the waveforms generated fully numerically with those computed by the perturbative (SRWZ) approach. Since our full numerical evolutions routinely extract the Weyl scalar ψ_4 at intermediate radii, typically around $R = 100M$ (a compromise between far enough of the sources and high enough local resolution), and the perturbative code evolves the Regge-Wheeler and Zerilli waveforms, we need to translate these different measurements of the waveform into a common radiation quantity. While analytic expressions already exist that relate them both [44], such expressions involve second derivatives that lead to some numerical noise when building up ψ_4, for instance. The usual strain h also involves two integration constants that are hard to fix with accuracy [9,49]. Hence, as a compromise, we use the *news* function, essentially dh/dt, which displays nicer smoothness properties for numerical comparisons.

In Figs. 7–9 we superpose the waveforms obtained for the full numerical evolution of the $q = 1/10$ black-hole binary case and the perturbative waveforms as computed by the integration of the wave equations (25) and (29) both, including the spin corrections ($a/M = 0.26$) or simply setting it to zero. We do these comparisons for the leading $(\ell, m) = (2, 2)$ mode and the next-to-leading $(2, 1)$ and $(3, 3)$ modes. Note that while $(2, 1)$ is an odd parity
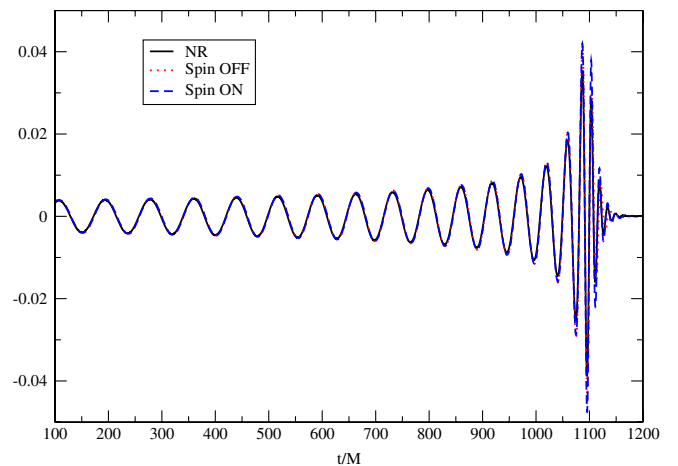

FIG. 7 (color online). The real part of the $(\ell = 2, m = 2)$ mode of dh/dt for the $q = 1/10$ case. The (black) solid, (red) dotted, and (blue) dashed curves show the NR, spin-off, and spin-on calculations, respectively.
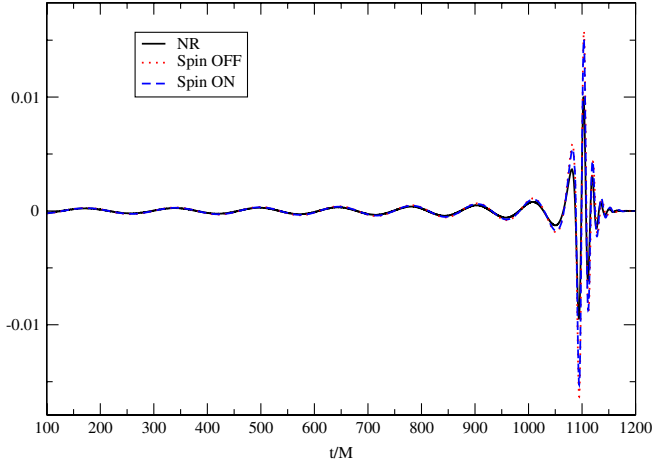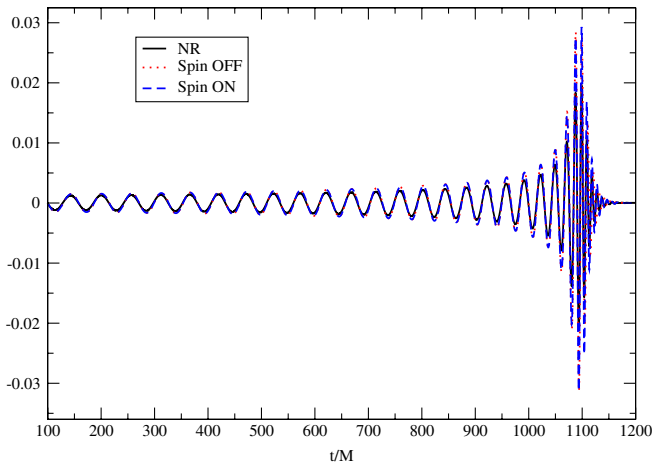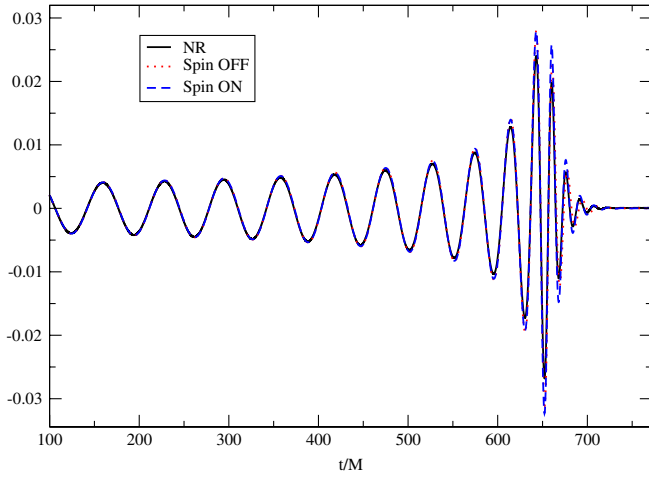
FIG. 8 (color online). The real part of the ($\ell = 2$, $m = 1$) mode of dh/dt for the $q = 1/10$ case. The (black) solid, (red) dotted, and (blue) dashed curves show the NR, spin-off, and spin-on calculations, respectively.

FIG. 9 (color online). The real part of the ($\ell = 3$, $m = 3$) mode of dh/dt for the $q = 1/10$ case. The (black) solid, (red) dotted, and (blue) dashed curves show the NR, spin-off, and spin-on calculations, respectively.

mode (for $a = 0$) and comes from integration of the Regge-Wheeler equation (23), the other modes are even parity and hence obtained by integration of the Zerilli equation (22). In all cases we use the same "full numerical" trajectory.

When spin terms are switched on, there is a coupling of even and odd parity modes as shown in Eqs. (25) and (29).

We have computed the overlap functions, as defined in Ref. [9], of these three sets of waveforms in order to quantify the phase agreement between them. This provides some insight into the possibility of using these perturbative waveforms to build up a bank of templates to support detection and analysis of gravitational wave observatories such as LIGO and VIRGO. Table IV shows that the agreement between numerical and perturbative waveforms is very good in general for all three modes, and that including the spin dependence improves the matching to an excellent level. This improvement is based on the accurate description of the late time phase, as we will discuss next, and is independent of the particle's track. The orbital (inspiral) part of the waveforms are not so strongly dependent on the spin terms (for our simulations) and are correctly described by the nonspinning perturbations. It is interesting to note here that the excellent phase agreement during the inspiral orbit might not be so surprising since the perturbative code uses the full numerical tracks (transformed into Schwarzschild coordinates); however, coordinates and gauges in full numerical evolutions are described in quite a different way than in (analytic) perturbative expressions, and it is reassuring to find such a good agreement in the final products of evolutions.

In Figs. 10–12 we superpose the waveforms for the modes (2, 2), (2, 1), and (3, 3) obtained from the full numerical evolution of the $q = 1/15$ case. We included full numerical, perturbative with spin ($a/M = 0.189$), and without spin corrections ($a = 0$). We computed the overlap functions, as defined in Ref. [9], for these three sets of waveforms and display the results in Table V. We observe again the generally very good agreement of the perturbative and full numerical waveforms. The agreement is still stronger when we include the spin dependence of the remnant black hole.

In order to study in more detail the agreement of the numerical and perturbative waveforms, we will proceed to decompose them into phase and amplitude (φ, A) with the usual formula

$$\psi = A \exp(i\varphi). \qquad (54)$$

TABLE IV. The overlap (matching) between the NR and perturbative dh/dt for the $q = 1/10$ case. The integration time is from $t/M = 100$ to 1220, and the definition of the matching is given in Eqs. (26) and (27) of [9].

| Mode	$\Re(\ell = 2, m = 2)$	$\Re(\ell = 2, m = 1)$	$\Re(\ell = 3, m = 3)$
Match (Spin OFF)	0.980 404	0.968 137	0.927 807
Match (Spin ON)	0.995 055	0.982 173	0.995 347
Mode	$\Im(\ell = 2, m = 2)$	$\Im(\ell = 2, m = 1)$	$\Im(\ell = 3, m = 3)$
Match (Spin OFF)	0.980 379	0.972 727	0.928 151
Match (Spin ON)	0.995 196	0.982 604	0.995 571

FIG. 10 (color online). The real part of the $(\ell = 2,\ m = 2)$ mode of dh/dt for the $q = 1/15$ case. The (black) solid, (red) dotted, and (blue) dashed curves show the NR, spin-off, and spin-on calculations, respectively.

FIG. 12 (color online). The real part of the $(\ell = 3,\ m = 3)$ mode of dh/dt for the $q = 1/15$ case. The (black) solid, (red) dotted, and (blue) dashed curves show the NR, spin-off, and spin-on calculations, respectively.
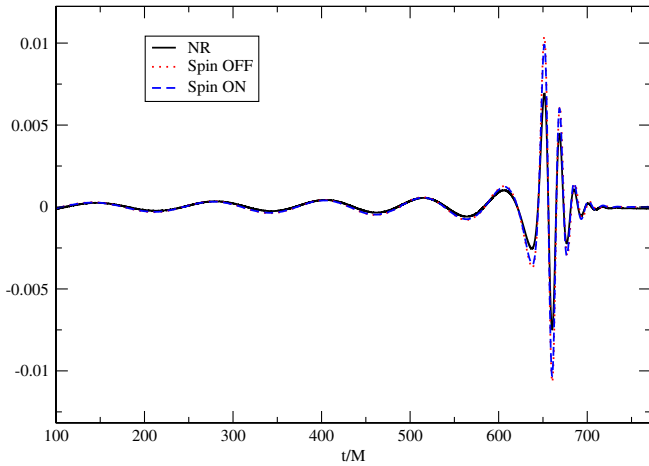
FIG. 11 (color online). The real part of the $(\ell = 2,\ m = 1)$ mode of dh/dt for the $q = 1/15$ case. The (black) solid, (red) dotted, and (blue) dashed curves show the NR, spin-off, and spin-on calculations, respectively.

We display in Figs. 13–15 the phases of the (2, 2), (2, 1) and (3, 3) modes for the $q = 1/10$ case. Note the very good agreement between numerical and perturbative waveforms for the whole range of the simulation. All the agreements
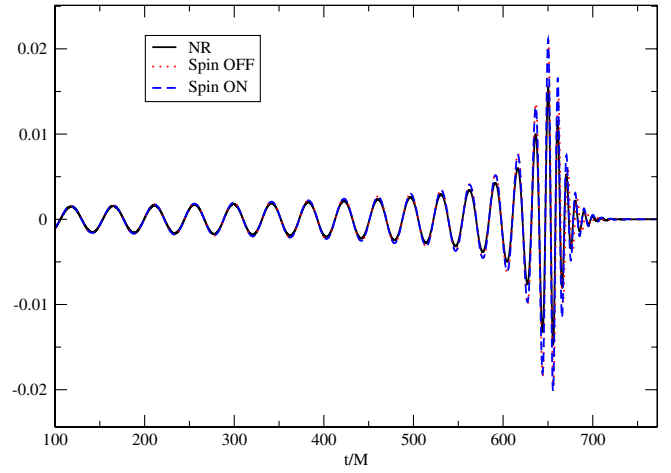
have been found with a single full numerical trajectory feeding the source terms of both the even and odd parity perturbative equations. The insets in the figures zoom in on the late time phases to display the effect of the spin correction, which in all three modes shows improvements over the nonspinning background case.

Figures 16–18 show the phases of the (2, 2), (2, 1) and (3, 3) modes for the $q = 1/15$ case. Again very good agreement is seen for the whole range of the full numerical simulation between perturbative and numerical results. The insets show that the spin correction, even if smaller than for the $q = 1/10$ case, still improves the late time phase, correctly capturing the quasinormal frequencies of the slowly rotating Kerr black hole ($a/M = 0.189$).

We now turn to compare amplitudes of waveforms. Although for gravitational wave detection by the LIGO and VIRGO observatories the most important indicator is the phase, the amplitude agreement is particularly important in the modeling of the sources. Figure 19 directly compares the amplitudes of the $q = 1/10$ and $q = 1/15$ cases, shifted in time to agree at the peaks of their amplitudes. We then rescale the amplitudes of the $q = 1/15$ waveform by the factor $\mu(q = 1/10)/\mu(q = 1/15) \approx 1.41$ to verify a linear rescaling. We find that the rescaled

TABLE V. The overlap (matching) between the NR and perturbative dh/dt for the $q = 1/15$ case. The integration time is from $t/M = 100$ to 750, and the definition of the matching is given in Eqs. (26) and (27) of [9].

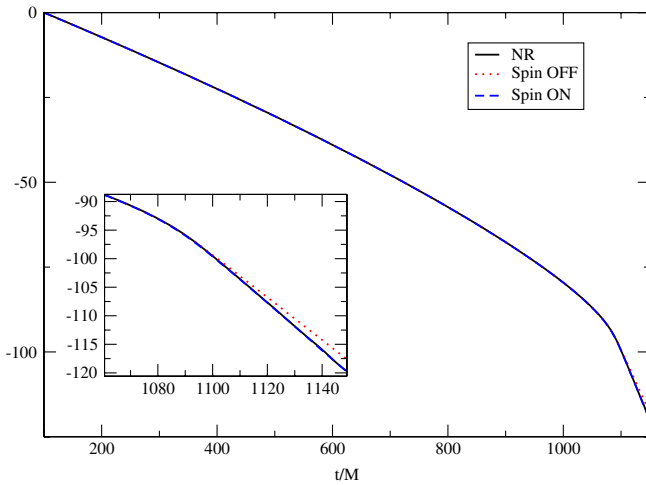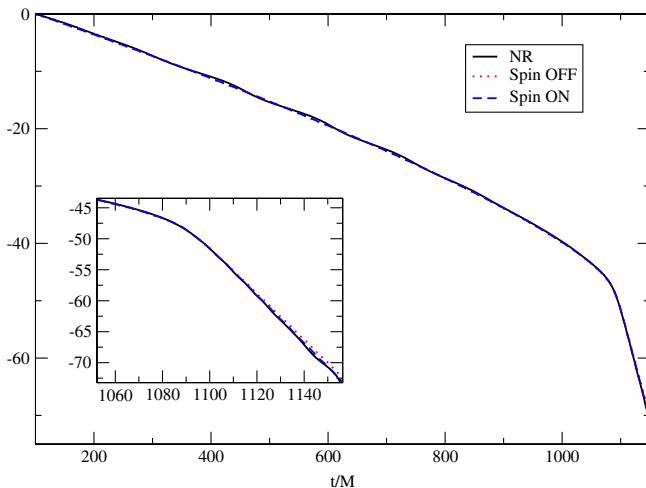| Mode	$\Re(\ell = 2,\ m = 2)$	$\Re(\ell = 2,\ m = 1)$	$\Re(\ell = 3,\ m = 3)$
Spin OFF	0.991 297	0.993 986	0.969 254
Spin ON	0.996 607	0.997 256	0.995 974
Mode	$\Im(\ell = 2,\ m = 2)$	$\Im(\ell = 2,\ m = 1)$	$\Im(\ell = 3,\ m = 3)$
Spin OFF	0.991 653	0.996 433	0.968 889
Spin ON	0.996 780	0.998 178	0.996 218

FIG. 13 (color online). The phase evolution of the ($\ell = 2$, $m = 2$) wave for the $q = 1/10$ case. The (black) solid, (red) dotted, and (blue) dashed curves show the NR, spin-off, and spin-on calculations, respectively. The inset shows the zoom-in for the quasinormal region.
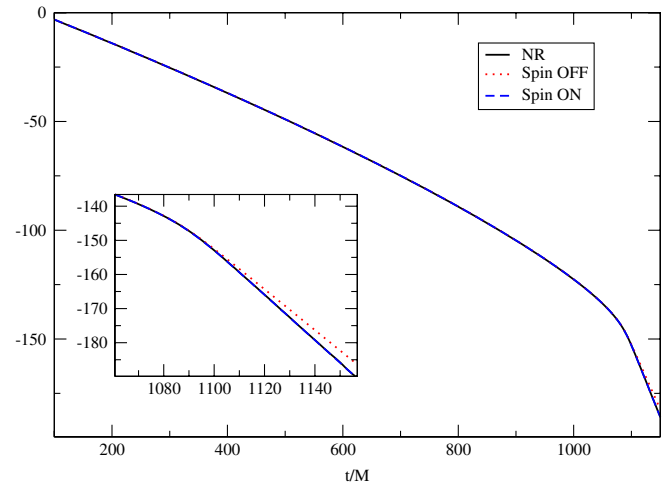

FIG. 15 (color online). The phase evolution of the ($\ell = 3$, $m = 3$) wave for the $q = 1/10$ case. The (black) solid, (red) dotted, and (blue) dashed curves show the NR, spin-off, and spin-on calculations, respectively. The inset shows the zoom-in for the quasinormal region.

amplitude of the $q = 1/15$ wave is very close to the actual $q = 1/10$ amplitude, showing that the systems are close to behaving linearly at these mass ratios.

In order to assess this last point in more detail, we compute the differences of the numerical and perturbative waveforms for each case, $q = 1/10$ and $q = 1/15$, and study how this "error" scales with q (or more precisely μ). We display the results of such computations in Figs. 20 and 21 for the cases of neglecting the spin of the final hole and that of taking it into account, respectively. The plots show that the inspiral phase scales like μ^2 as one would predict if the system would be completely linearized. While in the

final merger region, near the peak of the amplitude, the rescaled differences display a dependence in μ between linear and quadratic, as if there are still nonlinearities present. One would expect this behavior for values of q that are in the intermediate mass ratio regime, where the linear approximation is good but small nonlinear effects can still be observed.

V. DISCUSSION

In this paper we have described in detail the techniques used to compute gravitational waveforms with the
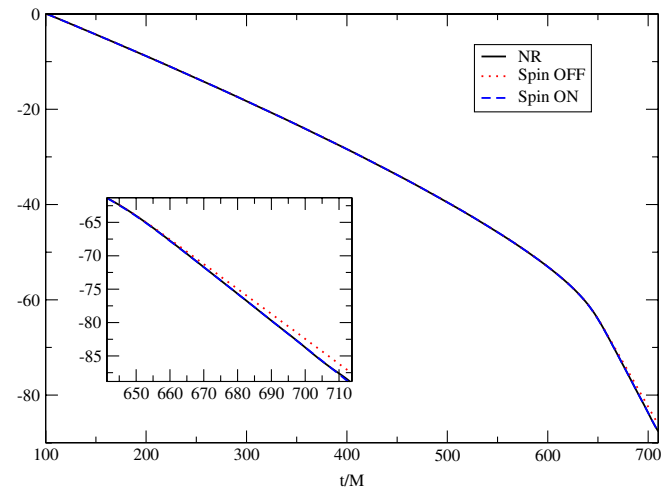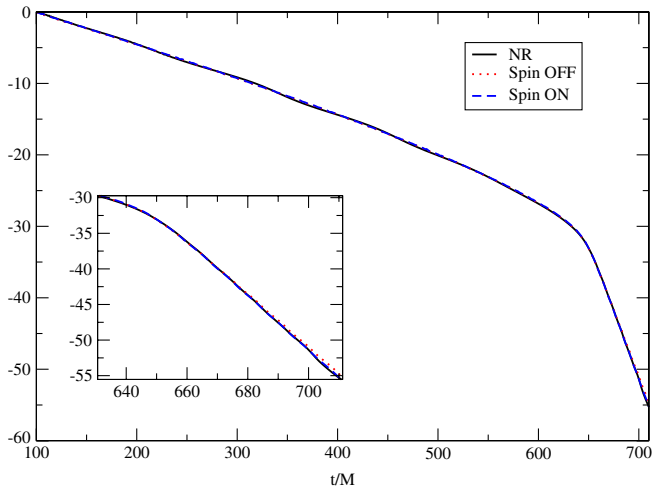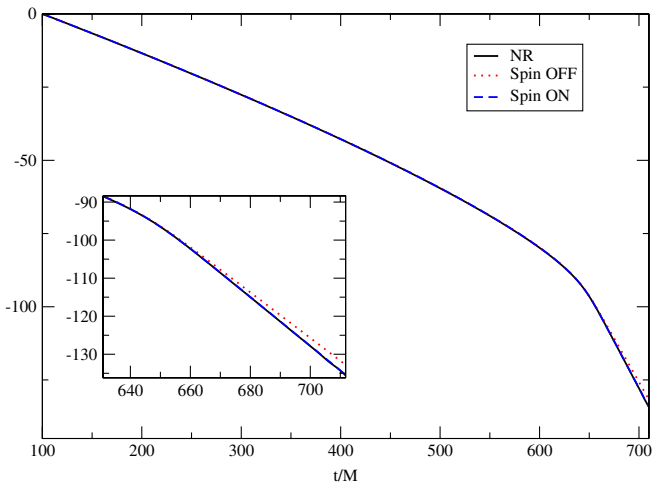

FIG. 14 (color online). The phase evolution of the ($\ell = 2$, $m = 1$) wave for the $q = 1/10$ case. The (black) solid, (red) dotted, and (blue) dashed curves show the NR, spin-off, and spin-on calculations, respectively. The inset shows the zoom-in for the quasinormal region.

FIG. 16 (color online). The phase evolution of the ($\ell = 2$, $m = 2$) wave for the $q = 1/15$ case. The (black) solid, (red) dotted, and (blue) dashed curves show the NR, spin-off, and spin-on calculations, respectively. The inset shows the zoom-in for the quasinormal region.
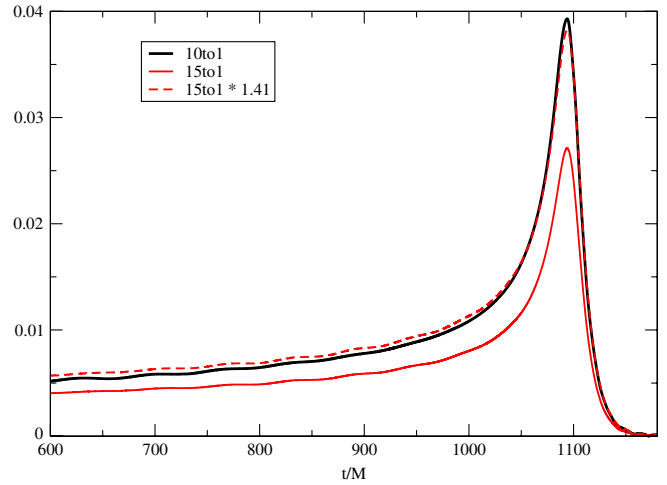
FIG. 17 (color online). The phase evolution of the ($\ell = 2$, $m = 1$) wave for the $q = 1/15$ case. The (black) solid, (red) dotted, and (blue) dashed curves show the NR, spin-off, and spin-on calculations, respectively. The inset shows the zoom-in for the quasinormal region.

FIG. 19 (color online). The amplitude of the ($\ell = 2$, $m = 2$) mode of the NR dh/dt for the $q = 1/10$ and $1/15$ cases. The (black) thick solid and (red) solid curves show the $q = 1/10$ and $1/15$ amplitudes, respectively. The (red) dashed curve denotes $\eta(q = 1/10)/\eta(q = 1/15) \sim 1.41$ times the $q = 1/15$ amplitude.

perturbative approach using full numerical trajectories in the source terms of the perturbative wave equations. The program was successfully tested in the $q = 1/10$ case in Ref. [11]. We have taken it further here studying larger initial separations for the full numerical evolutions of the $q = 1/10$ case, leading to simulations lasting for nearly eight orbits before the final plunge. We have also studied the case $q = 1/15$, the smallest mass ratio so far in the literature, in order to assess quantitatively the q-dependence of the agreement of the full numerical and perturbative evolutions in the intermediate mass ratio

regime. We have also included in our new computations the (linear dependence) spin of the final remnant in order to correctly reproduce the quasinormal ringing component of the full waveform at late times (after merger). The results are displayed in Tables IV and V and in Figs. 13–18. They show an apparent improvement in the matching (overlap) indices when the spin correction is taken into account compared to the vanishing spin case. In the Appendix we apply this linear-in-spin perturbation theory (SRWZ) to compute the corresponding quasinormal modes and
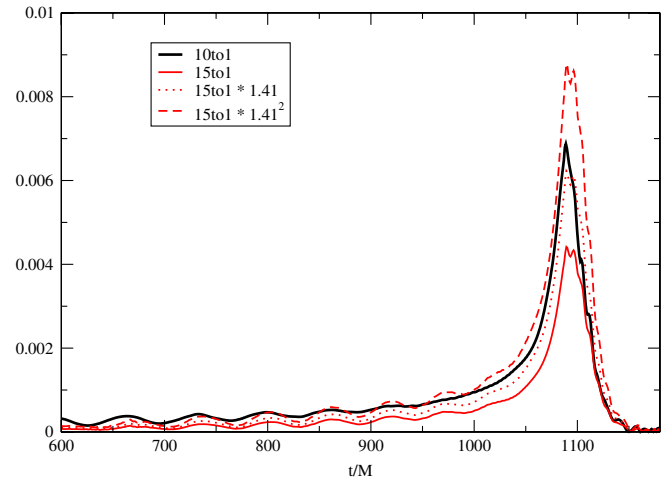

FIG. 18 (color online). The phase evolution of the ($\ell = 3$, $m = 3$) wave for the $q = 1/15$ case. The (black) solid, (red) dotted, and (blue) dashed curves show the NR, spin-off, and spin-on calculations, respectively. The inset shows the zoom-in for the quasinormal region.

FIG. 20 (color online). The amplitude difference in the ($\ell = 2$, $m = 2$) mode between the NR and perturbative dh/dt for the spin-off cases. The (black) thick solid curve shows the $q = 1/10$ case. The (red) solid, dotted, and dashed curves show the amplitude differences for the $q = 1/15$ case rescaled by factors of 1, 1.41, and 1.41^2, respectively.
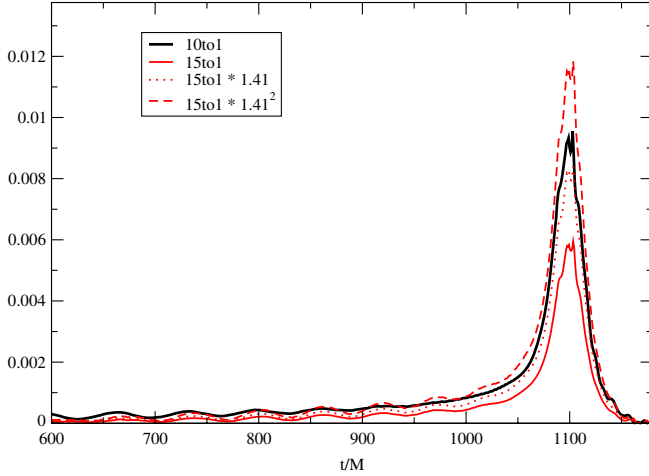
FIG. 21 (color online). The amplitude difference in the ($\ell = 2$, $m = 2$) mode between the NR and perturbative dh/dt for the spin-on cases. The (black) thick solid curve shows the $q = 1/10$ case. The (red) solid, dotted, and dashed curves show the amplitude differences for the $q = 1/15$ case rescaled by factors of 1, 1.41, and 1.41^2, respectively.

compare the frequencies of these modes with those obtained for a Kerr black hole background for all values of the spin parameter. We observe the results in Figs. 29 and 30. They show that SRWZ provide reliable predictions for $a/M \lesssim 0.3$, which justifies their use for the cases studied here where $a/M = 0.26, 0.19$ for $q = 1/10, 1/15$, respectively. The generalization to arbitrary spins requires solving the Teukolsky equation instead of the RWZ ones [50]. Note that the relevant spin-effects on the waveforms are due to the spin of the large black hole, while the effects of the spin of the small hole on radiation will tend to be negligible as q decreases. The use of numerical trajectories to describe the motion of the small hole in the field of the larger one already incorporates the spin dependence where the effects are stronger.

After comparing the perturbative and full numerical waveforms and verifying the accuracy of the former, there remains the question of accurately modeling the trajectories for small q BHBs. We have stressed here an important fact, that the trajectory dependence disappears from the perturbative formulation once the black holes merge, reducing the need of further full numerical simulations with the resulting saving of computational resources. This savings is not negligible, because one saves not only the (relatively short) time of evolution from merger to the end of the ringdown, but also the evolution time required to propagate the signal to an observer located far away from the sources. Typically, this should save over $500M$ of full numerical evolution. One can also predict the parameters of the final black hole by using formulae for the remnant parameters, as in [51,52], found by empirical fitting. Still, the goal of our project is to be able to model, empirically, the BHBs inspiral trajectories as a function

of q from a reasonably small number of full numerical evolutions. In particular, numerical evolutions start from a finite, relatively close initial separation of the holes. It is hence important to provide the large separation input from PN theory. While the full modeling of trajectories is beyond the scope of the current paper, here we discuss how this interface can be achieved for the current simulations of the $q = 1/10$ and $q = 1/15$ cases. The results are summarized in Figs. 22 and 23. We have considered the full numerical and PN trajectories in the Schwarzschild coordinates, i.e., correct the full numerical tracks for the $1 +$ log time slice and the PN ones for the quasiisotropic coordinates (ADM-TT gauge). In the $q = 1/10$ case, the full numerical evolutions essentially start from initial separations $R_i \approx 9.5M$ in the Schwarzschild coordinates. We see a relatively smooth matching for the tracks and their first derivative in the upper-left inset of Fig. 22. This would lead hence to smooth waveforms in the whole range of the evolution, i.e., from as large initial (PN) separations as needed down to the ringdown. Note, however, that in order to achieve this smooth matching of trajectories we had to make use of the resummed PN (RPN) evolutions (i.e. containing exactly the particle limit in the Schwarzschild background). The RPN Hamiltonian used here is derived in the following. Based on the Hamiltonian formulation for the test particle given in [53], the resummed part H_{Sch} is calculated by using the Schwarzschild metric in the isotropic coordinates. Then the RPN Hamiltonian is given by

$$H^{\text{RPN}} = H_{\text{Sch}} + \tilde{H}_{\text{1PN}} + \tilde{H}_{\text{2PN}} + \tilde{H}_{\text{3PN}}. \quad (55)$$
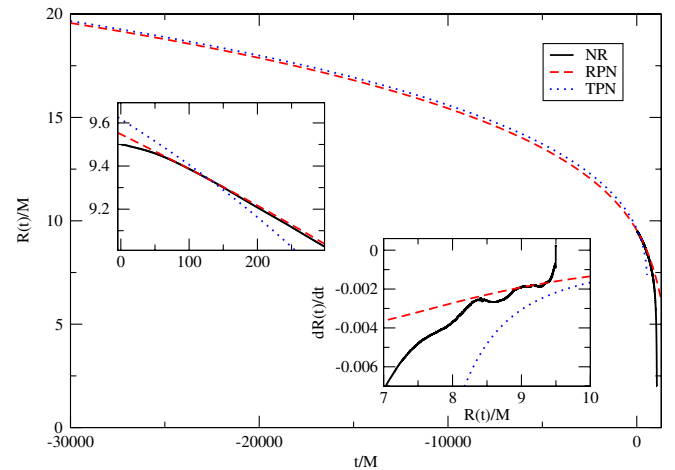

FIG. 22 (color online). The radial trajectory $R(t)$ obtained from the PN and NR evolutions for the $q = 1/10$ case in the Schwarzschild coordinates. The (black) solid, (red) dashed, and (blue) dotted curves show the NR, resummed, and Taylor PN ones, respectively. From the lower-right inset, we can choose the matching radius between the NR and resummed PN evolutions as $R(t)/M = 9.35123$. The upper-left inset is the zoom-in around the matching time.
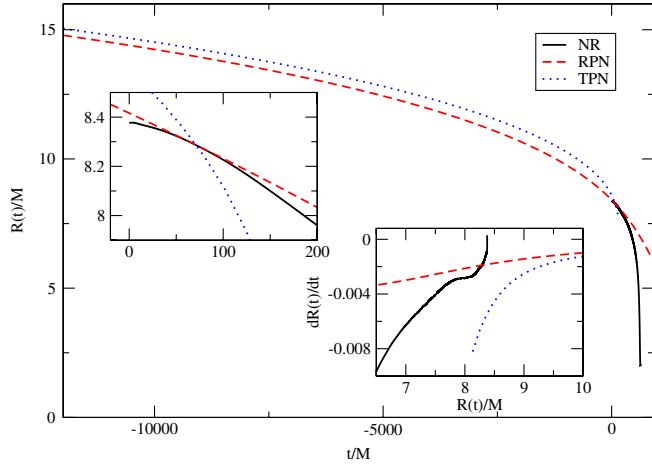
FIG. 23 (color online). The radial trajectory $R(t)$ obtained from the PN and NR evolutions for the $q = 1/15$ case in the Schwarzschild coordinates. The (black) solid, (red) dashed, and (blue) dotted curves show the NR, resummed, and Taylor PN ones, respectively. From the lower-right inset, we can choose the matching radius between the NR and resummed PN evolutions as $R(t)/M = 8.287\,96$. The upper-left inset is the zoom-in around the matching time.

The finite mass effects $\tilde{H}_{1PN}$, $\tilde{H}_{2PN}$, and $\tilde{H}_{3PN}$ in the above Hamiltonian are introduced by the result of the standard 3PN Taylor Hamiltonian (TPN) and the 3.5PN radiation reaction effects on the equations of motion are treated as in [54]. In practice, $\tilde{H}_{nPN}$ is obtained by the subtraction of the test particle limit from the Taylor PN Hamiltonian H_{nPN}. The PN evolutions in the figures have been obtained from the quasicircular initial parameter at $R(t) \sim 50M$. A good matching, at this initial separation, cannot be achieved with the TPN Hamiltonian. Of course, at larger separations both PN expressions get closer to each other, and a full numerical simulation started at such large initial separations could be matched by Taylor PN expansion as well.

This also suggests that, at even closer separations, as in the case of the numerical evolutions for $q = 1/15$ starting from $R_i \approx 8.4M$, not even the resummed PN leads to a very smooth matching of track. This is indeed the case displayed in Fig. 23. We may then conclude that, in order to simulate full inspirals of $q \sim 1/10$ matched to resummed PN, one needs to start the full numerical simulations from initial separations $R_i > 9M$ in the Schwarzschild coordinates, i.e., $R_i^{(QI)} > 8M$ in the quasiisotropic coordinates. Alternatively, one could seek to improve the resummed PN expansions with the effective one-body (EOB) formalism [55] and its extension to incorporate full numerical results (EOBNR) [56]. It is also relevant to cite here the works [57–59] that make perturbative evolutions of particle trajectories completely derived from PN expansions and used all the way down to merger without direct input from full numerical trajectories.

If one can indeed extend those improved post-Newtonian treatments down to the ISCO in the particle limit, at $R = 6M$ in the Schwarzschild coordinates, i.e., $R^{(ISCO)} \approx 4.95M$ in the isotropic coordinates, then one can argue that the subsequent merger trajectory reaches a "universal" limit given by the geodesic motion of quasicircular orbits. In fact this seems to be the case for the tracks of the $q = 1/10$ and $q = 1/15$ simulations as displayed in Fig. 3. One can argue that the very low level of radiation of those plunging orbits implies the universal form of the track. This was also recently observed in [59] studying PN orbits. Notably, at the other extreme of the mass ratio range, i.e., for equal (and comparable) mass BHBs, the strong gravitational emission taking place during the plunge erases any details of the preliminary evolution and one observes a universal waveform [60–63]

To see the universal behavior of geodesics inside the ISCO for quasicircular inspirals, we use the orbits with imaginary eccentricities for timelike geodesics in the Schwarzschild spacetime as given on page 111 of [64]. The initial part of these orbits can be considered the continuation of the inspiral trajectories through the ISCO. These geodesics have the following form near the horizon:

$$\Phi(R) \sim \frac{3}{4}\sqrt{6}\left[\left(1 - \frac{1}{8}e^2 + \frac{3}{8}\left(1 - \frac{R_0}{6M}\right)^2\right)\left(\frac{R}{2M} - 1\right) \right. $$
$$\left. + \left(\frac{1}{8} - \frac{13}{64}e^2 + \frac{39}{64}\left(1 - \frac{R_0}{6M}\right)^2\right)\left(\frac{R}{2M} - 1\right)^2\right], \quad (56)$$

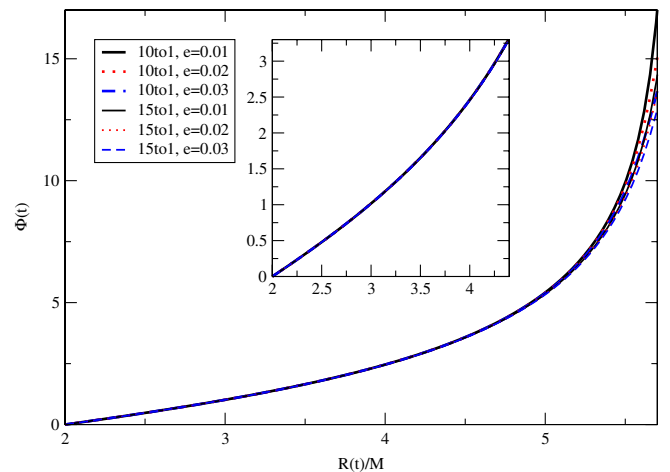where the imaginary eccentricity (*ie*) is a small quantity, and $R_0 < 6M$.

FIG. 24 (color online). The orbit with imaginary eccentricities discussed in [64]. The thick and thin curves show the $q = 1/10$ and $q = 1/15$ cases, respectively. Here we show the orbits with various eccentricities.

The initial velocity at $R(t) = R_0$ is approximately given by

$$\frac{dR(t)}{dt} = -\frac{\sqrt{6}}{6}e\sqrt{\left(1 - \frac{R_0}{6M}\right)},$$

$$\frac{d\Phi(t)}{dt} = \frac{\sqrt{6}}{36M} + \frac{\sqrt{6}}{24M}\left(1 - \frac{R_0}{6M}\right)$$
$$+ \frac{\sqrt{6}}{288M}\left(15\left(1 - \frac{R_0}{6M}\right)^2 - e^2\right), \quad (57)$$

which allows us to match to full numerical trajectories and then use the geodesic expressions to smoothly suppress the local source terms when the particle approaches the Schwarzschild horizon (See Sec. III A 4).

In Fig. 24, we plot the phase evolution in terms of the orbital radius. As a fiducial starting point, just inside the Schwarzschild ISCO, we take the self-force corrected ISCO radius

$$R_0 = 6M - 3.269\mu, \quad (58)$$

as discussed in [65]. Although we see some differences in the initial part of the orbits, the trajectories reach a universal limit approaching the horizon.

ACKNOWLEDGMENTS

APPENDIX: ANALYSIS OF THE WAVE EQUATIONS

The following is useful for the analytic discussion, especially the behavior of the source term around the horizon. And this also gives a stable evolution in the numerical calculation, because nonvanishing contributions at the horizon in the source terms are canceled out analytically.

Here, we discuss the wave functions as

$$\Psi_{\ell m}(t, r) = \Psi_{\ell m}^{(in)}(t, r)\theta(R(t) - r) + \Psi_{\ell m}^{(out)}(t, r)\theta(r - R(t)),$$

$$\Psi_{\ell m}^{(step)}(t, r) = \Psi_{\ell m}^{(out)}(t, r) - \Psi_{\ell m}^{(in)}(t, r), \quad (A1)$$

where $\Psi_{\ell m}$ denotes the even or odd parity wave function. The functions $\Psi_{\ell m}^{(in)}$, $\Psi_{\ell m}^{(out)}$, and $\Psi_{\ell m}^{(step)}$ are the homogene-

ous solutions of the Regge-Wheeler-Zerilli equations. From these definitions, we have

$$\Psi_{\ell m}(t, r) = \Psi_{\ell m}^{(in)}(t, r) + \Psi_{\ell m}^{(step)}(t, r)\theta(r - R(t)). \quad (A2)$$

Therefore, for example, the time derivative of the above wave function is written as

$$\partial_t \Psi_{\ell m}(t, r) = \partial_t \Psi_{\ell m}^{(in)}(t, r) + (\partial_t \Psi_{\ell m}^{(step)}(t, r))\theta(r - R(t))$$
$$- \Psi_{\ell m}^{(step)}(t, r)\frac{dR(t)}{dt}\delta(r - R(t))$$
$$= \partial_t \Psi_{\ell m}^{(in)}(t, r) + (\partial_t \Psi_{\ell m}^{(step)}(t, r))\theta(r - R(t))$$
$$- \Psi_{\ell m}^{(step)}(t, R(t))\frac{dR(t)}{dt}\delta(r - R(t)). \quad (A3)$$

To find the quantities of the waveforms at the particle location, i.e., $\Psi_{\ell m}^{(step)}(t, R(t))$, we use

$$\partial_t \Psi_{\ell m}^{(1)}(t, r) = \Psi_{\ell m}^{(Z, 1)}(t, r) + \frac{16\sqrt{2}\pi i r^2(r - 2M)}{\ell(\ell + 1)(r\ell^2 + r\ell - 2r + 6M)}$$
$$\times \mathcal{A}_{1\ell m}^{(1)}(t, r),$$

$$\partial_t \Psi_{\ell m}^{(o, 1)}(t, r) = 2\Psi_{\ell m}^{(o, Z, 1)}(t, r) + \frac{16\sqrt{2}\pi i r(r - 2M)}{(\ell - 1)(\ell + 2)\sqrt{\ell(\ell + 1)}}$$
$$\times \mathcal{Q}_{\ell m}^{(1)}(t, r), \quad (A4)$$

where each wave function in the left-hand and right-hand side of the above equations behaves as a step function at the particle's location because of the first-order Regge-Wheeler-Zerilli waveforms. Therefore, substituting Eq. (A3) into $\partial_t \Psi_{\ell m}^{(1)}$ and $\partial_t \Psi_{\ell m}^{(o, 1)}$, we obtain the analytic expression of $\Psi_{\ell m}^{(step)}(t, R(t))$ from the coefficients of the Dirac's delta function.

1. Analysis of the even parity wave equation

We have introduced a new function for the even parity calculation to the SRWZ formalism:

$$\Psi_{\ell m}(t, r) = \Psi_{\ell m}^{(1)}(t, r) + \Psi_{\ell m}^{(2)}(t, r). \quad (A5)$$

The gravitational waveform with the spin effect is obtained directly from $\Psi_{\ell m}$. Therefore, we discuss the wave equation for $\Psi_{\ell m}$ in the following. Here, we create our numerical code for the perturbative calculation based on [31]. It is important to distinguish the cell that the particle does cross from the other cells.

For the cell that the particle does not cross, we use the following homogeneous equation, i.e., can read the following equation from the step function part, which does not include the local source term:

$$-\frac{\partial^2}{\partial t^2}\Psi_{\ell m}(t,r) + \frac{(r-2M)^2}{r^2}\frac{\partial^2}{\partial r^2}\Psi_{\ell m}(t,r) + 2\frac{(r-2M)M}{r^3}\frac{\partial}{\partial r}\Psi_{\ell m}(t,r) - (r-2M)(4r^3\ell - \ell^4 r^3 + 3\ell^5 r^3 - 7\ell^3 r^3$$

$$+ \ell^6 r^3 + 12\ell^3 r^2 M - 24r^2 M\ell - 18r^2 M\ell^2 + 24r^2 M + 6\ell^4 r^2 M - 72rM^2 + 36\ell^2 rM^2 + 36\ell rM^2$$

$$+ 72M^3)\Psi_{\ell m}(t,r)/[(r\ell^2 + \ell r - 2r + 6M)^2 r^4] - 4iSm(4r^3\ell^7 + 144M^3\ell^2 + 16r^3\ell - 24r^3 + 18M\ell^6 r^2$$

$$+ 144M^3\ell + r^3\ell^8 - 216rM^2 - 66\ell^3 r^2 M - 48r^2 M\ell + 144M^3 + 36\ell^2 rM^2 + 22r^3\ell^2 + 120r^2 M + 6\ell^3 r^3$$

$$- 11\ell^4 r^3 + 54Mr^2\ell^5 + 72M^2\ell^4 r + 12\ell^4 r^2 M + 144M^2 r\ell^3 - 90r^2 M\ell^2 - 36\ell rM^2$$

$$- 14\ell^5 r^3)\frac{\partial}{\partial t}\Psi_{\ell m}(t,r)/[r^3(\ell+1)\ell(r\ell^2 + \ell r - 2r + 6M)^3] + \frac{24iS(\ell+2)(\ell-1)m(r-2M)^2}{r^2(r\ell^2 + \ell r - 2r + 6M)^2\ell(\ell+1)}\frac{\partial^2}{\partial t\partial r}\Psi_{\ell m}(t,r)$$

$$= -12S\sqrt{\frac{(\ell-m)(\ell+m)}{(2\ell-1)(2\ell+1)}}(r-2M)(\ell-2)(\ell^5 r^2 + 2r^2\ell^4 + 4r\ell^3 M - 4r^2\ell^2 + 12rM\ell^2 - 5r^2\ell + 12rM\ell$$

$$+ 6r^2 - 28rM + 36M^2)\Psi^{(o)}_{\ell-1m}(t,r)/[r^5\ell(r\ell^2 + \ell r - 2r + 6M)^2]$$

$$+ 12S\sqrt{\frac{(\ell+m+1)(\ell-m+1)}{(2\ell+1)(2\ell+3)}}(r-2M)(\ell+3)(\ell^5 r^2 + 3r^2\ell^4 + 4r\ell^3 M + 2r^2\ell^3 + 2r^2\ell^2$$

$$+ 32rM - 8r^2 - 36M^2)\Psi^{(o)}_{\ell+1m}(t,r)/[(\ell+1)r^5(r\ell^2 + \ell r - 2r + 6M)^2]. \tag{A6}$$

And then we need the following local source term which is added to the right-hand side of the above equation, for the cell that the particle does cross:

$$S_{\ell m}^{(\text{even},\text{L})} = S_{\ell m}^{(\text{even},1,\text{L})} + S_{\ell m}^{(\text{even},2,\text{L})}, \tag{A7}$$

where the first-order source term $S_{\ell m}^{(\text{even},1,\text{L})}$ is the same as $S_{\ell m}^{(\text{even},1)}$ in Section III B 1 and given in Eq. (A.5) of [31] as

$$S_{\ell m}^{(\text{even},1,\text{L})} = \left[\frac{32\pi\mu(R(t)-2M)(2M-R(t)-\dot{R}(t)R(t))(2M-R(t)+\dot{R}(t)R(t))U(t)}{\ell(\ell+1)(R(t))^2(R(t)\ell^2 + R(t)\ell - 2R(t) + 6M)}\frac{d}{dr}\delta(r-R(t))\right.$$

$$+ \frac{\pi\mu}{\ell(\ell+1)}\left(\frac{32m^2(R(t)-2M)U(t)(\dot{\Phi}(t))^2}{(\ell-1)(\ell+2)} - \frac{64im\dot{R}(t)(R(t)-2M)U(t)\dot{\Phi}(t)}{R(t)\ell^2 + R(t)\ell - 2R(t) + 6M}\right.$$

$$- \frac{16(R(t)-2M)U(t)(\dot{\Phi}(t))^2}{(R(t)\ell^2 + R(t)\ell - 2R(t) + 6M)(\ell-1)(\ell+2)}(-8M + 10M\ell^2 + 10M\ell - 3R(t)\ell^2 + 2R(t)\ell^3 + 4R(t)$$

$$+ R(t)\ell^4 - 4R(t)\ell) + \frac{16U(t)(\dot{R}(t))^2}{R(t)(R(t)\ell^2 + R(t)\ell - 2R(t) + 6M)^2}(-2(R(t))^2\ell - (R(t))^2\ell^2 + 2\ell^3(R(t))^2 + \ell^4(R(t))^2$$

$$+ 12R(t)\ell^2 M + 12R(t)\ell M + 12M^2) - \frac{16(R(t)-2M)^2 U(t)}{(R(t))^3(R(t)\ell^2 + R(t)\ell - 2R(t) + 6M)^2}$$

$$\times (60M^2 + 12R(t)\ell^2 M - 24R(t)M + 12R(t)\ell M - 2(R(t))^2\ell - (R(t))^2\ell^2 + 2\ell^3(R(t))^2$$

$$\left.\left.+ \ell^4(R(t))^2\right)\right)\delta(r-R(t))\right]Y^*_{\ell m}(\Theta_0, \Phi(t)). \tag{A8}$$

The second-order local source term $S_{\ell m}^{(\text{even},2,\text{L})}$ has the following expression:

$$S_{\ell m}^{(\text{even},2,\text{L})} = \frac{192 i m S \pi \mu U(t)(R(t) - 2M)\dot{R}(t)(\ell^2 + \ell - 2m^2)(\dot{\Phi}(t))^2}{(\ell + 2)(\ell - 1)(\ell + 1)^2 \ell^2 (R(t)\ell^2 + R(t)\ell - 2R(t) + 6M)} Y_{\ell m}^*(\Theta_0, \Phi(t)) \frac{d}{dr} \delta(r - R(t))$$

$$+ \left[\frac{-24 i m S(\ell + 2)(\ell - 1)(R(t) - 2M)^2}{(R(t))^2 (R(t)\ell^2 + R(t)\ell - 2R(t) + 6M)^2 \ell(\ell + 1)} \frac{\partial}{\partial t} \Psi_{\ell m}^{(\text{step})}(t, r)\big|_{r = R(t)} + i m S \pi \mu Y_{\ell m}^*(\Theta_0, \Phi(t)) \right.$$

$$\times \left(-384(\ell^2 + \ell - 2m^2)(30M^2 + 6R(t)\ell^2 M + 6R(t)\ell M - 21R(t)M - 2\ell(R(t))^2 - 2\ell^2(R(t))^2 \right.$$

$$+ 4(R(t))^2) U(t)(\dot{\Phi}(t))^2 \dot{R}(t)/[R(t)(\ell + 2)(\ell - 1)(\ell + 1)^2 \ell^2 (R(t)\ell^2 + R(t)\ell - 2R(t) + 6M)^2]$$

$$- 128(R(t) - 2M) U(t)\dot{R}(t)((R(t))^2\ell^4 + 2(R(t))^2\ell^3 - 6\ell^2(R(t))^2 + 18R(t)\ell^2 M - 7\ell(R(t))^2 + 18R(t)\ell M$$

$$+ 10(R(t))^2 - 36R(t)M + 36M^2)/[\ell(R(t))^3 (R(t)\ell^2 + R(t)\ell - 2R(t) + 6M)^3 (\ell + 1)]$$

$$+ \frac{192 i m U(t)(\ell^2 + \ell - 2m^2)(R(t) - 2M)(\dot{\Phi}(t))^3}{(\ell + 2)(\ell - 1)(\ell + 1)^2 \ell^2 (R(t)\ell^2 + R(t)\ell - 2R(t) + 6M)} + 128 i m U(t)(R(t) - 2M)^2 (72M^2 + 30R(t)\ell^2 M$$

$$+ 30R(t)\ell M - 60R(t)M - 10\ell(R(t))^2 + (R(t))^2\ell^4 + 2(R(t))^2\ell^3 + 16(R(t))^2$$

$$\left. \left. - 9\ell^2(R(t))^2)\dot{\Phi}(t)/[(\ell + 1)^2 \ell^2 (R(t)\ell^2 + R(t)\ell - 2R(t) + 6M)^3 (R(t))^3] \right) \right] \delta(r - R(t))$$

$$+ \left(256\pi\mu S \sqrt{\frac{(\ell - m)(\ell + m)}{(2\ell - 1)(2\ell + 1)}} \frac{U(t)\dot{\Phi}(t)(R(t) - 2M)^2(-2R(t) + R(t)\ell + R(t)\ell^2 + 3M)}{\ell^2(\ell + 1)(R(t))^3 (R(t)\ell^2 + R(t)\ell - 2R(t) + 6M)^2} \partial_\theta Y_{\ell - 1 m}^*(\Theta_0, \Phi(t)) \right.$$

$$- 256\pi\mu S \sqrt{\frac{(\ell + m + 1)(\ell - m + 1)}{(2\ell + 1)(2\ell + 3)}} \frac{U(t)\dot{\Phi}(t)(R(t) - 2M)^2(-2R(t) + R(t)\ell + R(t)\ell^2 + 3M)}{\ell(\ell + 1)^2 (R(t))^3 (R(t)\ell^2 + R(t)\ell - 2R(t) + 6M)^2}$$

$$\left. \times \partial_\theta Y_{\ell + 1 m}^*(\Theta_0, \Phi(t)) \right) \delta(r - R(t)). \tag{A9}$$

Here we have used the analytic expression of the wave function $\Psi_{\ell m}^{(\text{step})}(t, R(t))$ at the particle's location, and the instantaneous geodesic approximation for the second-order source term.

It is noted that there are remaining terms at the horizon in the integration of the wave equation. These arise from the transformation of the original wave equation to the above equation. Since the source term for the original wave equation does not include any remaining term at the horizon, these remaining terms cancel out with the derivatives of the wave function, i.e., $\partial \Psi_{\ell m}^{(\text{step})}/\partial t$.

2. Analysis of the odd parity wave equation

In the calculation for the odd parity perturbation of the SRWZ formalism, we have treated the first- and second-order perturbations separately. The first-order (local) source term, $S_{\ell m}^{(\text{odd},1,\text{L})} = S_{\ell m}^{(\text{odd},1)}$, which has been simplified with the geodesic equation, is given as

$$S_{\ell m}^{(\text{odd},1,\text{L})} = \frac{32\pi\mu}{\ell(\ell + 1)(\ell - 1)(\ell + 2)} \left[\left(U(t)(R(t) - 2M)(R(t))^2(\dot{\Phi}(t))^3 + \frac{(R(t) - 2M)\dot{\Phi}(t)}{U(t)} \right) \frac{d}{dr} \delta(r - R(t)) \right.$$

$$+ \left((2R(t) - 7M)R(t)U(t)(\dot{\Phi}(t))^3 - i m \dot{R}(t)R(t)U(t)(\dot{\Phi}(t))^2 + \frac{(R(t) - 5M)\dot{\Phi}(t)}{R(t)U(t)} \right.$$

$$\left. \left. - \frac{2(R(t) - 2M)^2 U(t)\dot{\Phi}(t)}{(R(t))^2} \right) \delta(r - R(t)) \right] \partial_\theta Y_{\ell m}^*(\Theta_0, \Phi(t)). \tag{A10}$$

Next, we focus on the second-order wave equation. $\Psi_{\ell \pm 1 m}^{(1)}$ and $\Psi_{\ell m}^{(o,1)}$ have already been derived in the first-order calculation. For the cell that the particle does not cross, we may consider only the homogeneous part of the wave equation,

$$-\frac{\partial^2}{\partial t^2}\Psi_{\ell m}^{(o,Z,2)}(t,r) + \frac{\partial^2}{\partial r^{*2}}\Psi_{\ell m}^{(o,Z,2)}(t,r) - V_\ell^{(odd)}(r)\Psi_{\ell m}^{(o,Z,2)}(t,r)$$

$$= imS\Bigg(-2\frac{(2r\ell^3 - 5r\ell^2 + 18r - 6r\ell + r\ell^4 + 9M\ell^2 - 42M + 9\ell M)(r-2M)}{(\ell+1)r^7\ell}\Psi_{\ell m}^{(o,1)}(t,r)$$

$$-2\frac{(3r-8M)(r-2M)}{r^6}\frac{\partial}{\partial r}\Psi_{\ell m}^{(o,1)}(t,r) + 2\frac{(r-2M)^2}{r^5}\frac{\partial^2}{\partial r^2}\Psi_{\ell m}^{(o,1)}(t,r)\Bigg)$$

$$+\frac{4S}{\ell(\ell-1)}\sqrt{\frac{(\ell-m)(\ell+m)}{(2\ell-1)(2\ell+1)}}\Bigg(3\frac{(r-2M)^2(\ell-1)}{r^5}\frac{\partial^2}{\partial t\partial r}\Psi_{\ell-1m}^{(1)}(t,r)$$

$$+\frac{3}{2}\frac{(r-2M)(\ell-1)(\ell^4r^2 - 2r^2\ell^3 - r^2\ell^2 + 2r^2\ell + 6r\ell^2M - 6r\ell M - 12rM + 24M^2)}{r^6(r\ell^2 - r\ell - 2r + 6M)}\frac{\partial}{\partial t}\Psi_{\ell-1m}^{(1)}(t,r)\Bigg)$$

$$+\frac{4S}{(\ell+1)(\ell+2)}\sqrt{\frac{(\ell+m+1)(\ell-m+1)}{(2\ell+1)(2\ell+3)}}\Bigg(-3\frac{(r-2M)^2(\ell+2)}{r^5}\frac{\partial^2}{\partial t\partial r}\Psi_{\ell+1m}^{(1)}(t,r)$$

$$-\frac{3}{2}\frac{(r-2M)(\ell+2)(\ell^4r^2 + 6r^2\ell^3 + 11r^2\ell^2 + 6r^2\ell + 6r\ell^2M + 18r\ell M + 24M^2)}{r^6(r\ell^2 + 3r\ell + 6M)}\frac{\partial}{\partial t}\Psi_{\ell+1m}^{(1)}(t,r)\Bigg). \tag{A11}$$

The second-order local source terms, $S_{\ell m}^{(\text{odd},Z,2,L)}$, which we need for the cell that the particle does cross, is written as

$$S_{\ell m}^{(\text{odd},Z,2,L)} = imS\Bigg(2\frac{(R(t)-2M)^2}{(R(t))^5}\frac{\partial}{\partial r}\Psi_{\ell m}^{(o,1,\text{step})}(t,r)|_{r=R(t)} - \frac{32\pi\mu(\ell+3)(\ell-2)U(t)\dot{\Phi}(t)(R(t)-2M)^2}{(R(t))^5(\ell+1)^2\ell^2(\ell-1)(\ell+2)}$$

$$\times\partial_\theta Y_{\ell m}^*(\Theta_0,\Phi(t))\Bigg)\delta(r-R(t)) + \frac{4S}{\ell(\ell-1)}\sqrt{\frac{(\ell-m)(\ell+m)}{(2\ell-1)(2\ell+1)}}$$

$$\times\Bigg[\frac{12\pi\mu(\ell+2)(\ell^2-\ell-2m^2)(\dot{\Phi}(t))^2(-R(t)+2M)U(t)\dot{R}(t)}{(R(t))^2(\ell-2)\ell}Y_{\ell-1m}^*(\Theta_0,\Phi(t))\frac{d}{dr}\delta(r-R(t))$$

$$+\Bigg(\frac{3(R(t)-2M)^2(\ell-1)(\ell+2)(\ell+1)}{(R(t))^5}\frac{\partial}{\partial t}\Psi_{\ell-1m}^{(1,\text{step})}(t,r)|_{r=R(t)}$$

$$+\frac{\pi\mu(\ell+2)}{\ell}\Bigg(-\frac{12im(R(t)-2M)U(t)(\ell^2-\ell-2m^2)(\dot{\Phi}(t))^3}{(R(t))^2(\ell-2)} - \frac{12(5R(t)-14M)\dot{R}(t)U(t)(\ell^2-\ell-2m^2)(\dot{\Phi}(t))^2}{(R(t))^3(\ell-2)}$$

$$+\frac{96im(R(t)-2M)^3(\ell+1)U(t)\dot{\Phi}(t)}{(R(t))^5(R(t)\ell^2 - R(t)\ell - 2R(t) + 6M)} - \frac{48(R(t)-2M)^2(\ell+1)U(t)\dot{R}(t)(\ell-1)\ell}{(R(t))^5(R(t)\ell^2 - R(t)\ell - 2R(t) + 6M)}\Bigg)$$

$$\times Y_{\ell-1m}^*(\Theta_0,\Phi(t))\Bigg)\delta(r-R(t))\Bigg] + [\ell\leftrightarrow-\ell-1] \tag{A12}$$

where $[\ell\leftrightarrow-\ell-1]$ refers to an additional term obtained by replacing ℓ with $-\ell-1$ in all terms in Eq. (A12), starting from $\frac{4S}{\ell(\ell-1)}\cdots$ and subsequently replacing $\Psi_{-\ell-2m}^{(1,\text{step})}$ with $\Psi_{\ell+1m}^{(1,\text{step})}$ and $Y_{-\ell-2m}^*$ with $Y_{\ell+1m}^*$. The above source term is added to the right-hand side of the homogeneous part of the wave equation. It is found that the right-hand side of the equation vanishes at the horizon. Here, the instantaneous geodesic approximation has also been used in the above equation.

3. Analysis of quasinormal modes

In the SRWZ formalism, we discuss a special case where the $\ell=2$, $m=\pm2$ even or odd parity mode is dominant and couplings with the other modes can be ignored. Also, the perturbed Regge-Wheeler-Zerilli equations with the spin effect do not have the local source terms, i.e., we consider the homogeneous equation.

For the even parity part, we use the same equation as Eq. (A6) without the other mode coupling:

$$\Bigg[-\frac{\partial^2}{\partial t^2} + \frac{\partial^2}{\partial r^{*2}} - 6\frac{(r-2M)(4r^3 + 4r^2M + 6rM^2 + 3M^3)}{r^4(2r+3M)^2}\Bigg]\Psi_{2\pm2}(t,r) \pm \frac{8iS(r-2M)^2}{r^2(2r+3M)^2}\frac{\partial^2}{\partial r\partial t}\Psi_{2\pm2}(t,r)$$

$$\mp\frac{8iS(6r^3 + 46r^2M + 45rM^2 + 21M^3)}{r^3(2r+3M)^3}\frac{\partial}{\partial t}\Psi_{2\pm2}(t,r) = 0. \tag{A13}$$

For the odd parity part, we use a different equation from Eq. (A11). This is because, if we ignore the other mode coupling and the local source term, we can derive a simple equation by using only the Cunningham *et al.* waveform $\Psi_{2\pm2}^{(o)}$ (or the Zerilli waveform $\Psi_{2\pm2}^{(o,Z)}$). The $\ell = 2, m = \pm2$ odd parity wave equation with the spin effect becomes

$$\left[-\frac{\partial^2}{\partial t^2} + \frac{\partial^2}{\partial r^{*2}} - 6\frac{(r-M)(r-2M)}{r^4}\right]\Psi_{2\pm2}^{(o)}(t,r)$$
$$\pm \frac{2iS}{r^2}\frac{\partial^2}{\partial r \partial t}\Psi_{2\pm2}^{(o)}(t,r) \mp \frac{2iS(7r^2-17rM+8M^2)}{(r-2M)r^4}$$
$$\times \frac{\partial}{\partial t}\Psi_{2\pm2}^{(o)}(t,r) = 0. \tag{A14}$$

where we have introduced $\Psi_{2\pm2}^{(o)}(t,r) = \Psi_{2\pm2}^{(o,1)}(t,r) + \Psi_{2\pm2}^{(o,2)}(t,r)$.

We treat the above equations in the frequency domain,

$$\left[\omega^2 + \frac{d^2}{dr^{*2}} - 6\frac{(r-2M)(4r^3+4r^2M+6rM^2+3M^3)}{r^4(2r+3M)^2}\right]$$
$$\times \Psi_{2\pm2}(\omega;r) \pm \frac{8S\omega(r-2M)^2}{r^2(2r+3M)^2}\frac{d}{dr}\Psi_{2\pm2}(\omega;r)$$
$$\mp \frac{8S\omega(6r^3+46r^2M+45rM^2+21M^3)}{r^3(2r+3M)^3}\Psi_{2\pm2}(\omega;r)$$
$$= 0, \tag{A15}$$

$$\left[\omega^2 + \frac{d^2}{dr^{*2}} - 6\frac{(r-M)(r-2M)}{r^4}\right]\Psi_{2\pm2}^{(o)}(\omega;r)$$
$$\pm \frac{2S\omega}{r^2}\frac{d}{dr}\Psi_{2\pm2}^{(o)}(\omega;r) \mp \frac{2S\omega(7r^2-17rM+8M^2)}{(r-2M)r^4}$$
$$\times \Psi_{2\pm2}^{(o)}(\omega;r) = 0. \tag{A16}$$

For the nonspinning ($S = 0$) case of the above equations, we have already known the transformation between the Regge-Wheeler and Zerilli function. This is known as the Chandrasekhar transformation [64], given by

$$\Psi_{2\pm2}^{(o,1)}(t,r) = \left(6 + 9\frac{M^2(r-2M)}{r^2(2r+3M)}\right)\Psi_{2\pm2}^{(1)}(t,r)$$
$$+ 3M\left(1 - 2\frac{M}{r}\right)\frac{d}{dr}\Psi_{2\pm2}^{(1)}(t,r). \tag{A17}$$

Using this transformation, for example, we may solve only the Regge-Wheeler equation to obtain the quasinormal frequency.

In order to discuss a similar treatment up to $O(a^1)$ ($a = S/M$), first we consider the following transformation:

$$\Psi_{2\pm2}(\omega;r) = \exp\left(\pm\frac{2S\omega}{2r+3M}\right)\tilde{\Psi}_{2\pm2}(\omega;r),$$
$$\Psi_{2\pm2}^{(o)}(\omega;r) = \exp\left(\pm\frac{S\omega}{r-2M}\right)\tilde{\Psi}_{2\pm2}^{(o)}(\omega;r), \tag{A18}$$
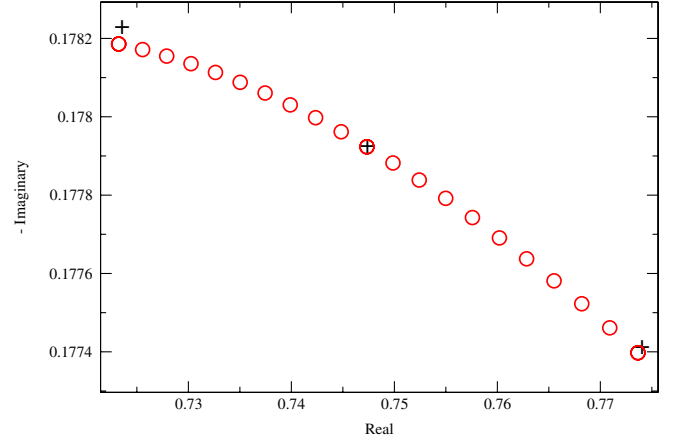

FIG. 25 (color online). The quasinormal frequencies, ω around $\chi = 0$. We have used the same expression as [67]. The (red) circles show our result, and the $+$ marks denote the values given in Table II of [68].

where these transformations are consistent in the $O(a^1)$. Since we treat the wave functions only up to $O(a^1)$, we may choose another transformation here. From the above transformations, we have the simple differential equations which are similar to the Regge-Wheeler and Zerilli equations. The difference from the original Regge-Wheeler and Zerilli equations arises in the potential terms.

$$\left[\omega^2 + \frac{d^2}{dr^{*2}} - 6\frac{(r-2M)(4r^3+4r^2M+6rM^2+3M^3)}{r^4(2r+3M)^2}\right]$$
$$\times \tilde{\Psi}_{2\pm2}(\omega;r) \mp \frac{8S\omega(4r^3+56r^2M+36rM^2+15M^3)}{r^3(2r+3M)^3}$$
$$\times \tilde{\Psi}_{2\pm2}(\omega;r) = 0, \tag{A19}$$
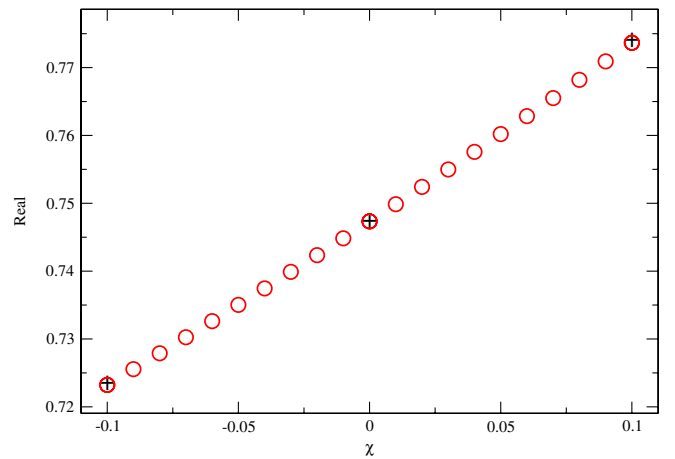

FIG. 26 (color online). The real part of the quasinormal frequencies, ω around $\chi = 0$. The horizontal axis denotes the nondimensional spin parameter, $\chi = S/M^2$. The (red) circles show our result, and the $+$ marks denote the values given in Table II of [68].
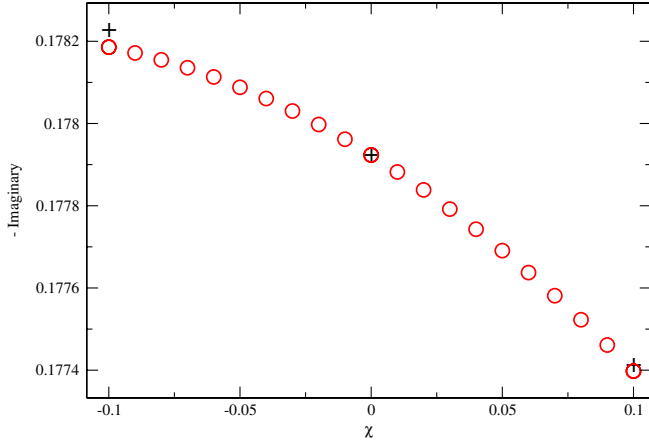
FIG. 27 (color online). The (minus) imaginary part of the quasinormal frequencies, ω around $\chi = 0$. The horizontal axis denotes the nondimensional spin parameter, $\chi = S/M^2$. The (red) circles show our result, and the $+$ marks denote the values given in Table II of [68].
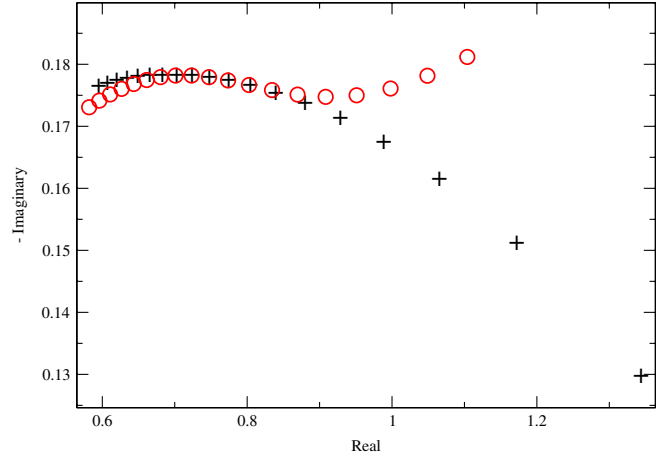

FIG. 28 (color online). The quasinormal frequencies, ω for $-0.9 \le \chi \le 0.9$. We have used the same expression as [67]. The (red) circles show our result, and the $+$ marks denote the values given in Table II of [68].

$$\left[\omega^2 + \frac{d^2}{dr^{*2}} - 6 \frac{(r-M)(r-2M)}{r^4} \right] \tilde{\Psi}_{2\pm2}^{(o)}(\omega; r)$$
$$\mp \frac{4S\omega(3r-2M)}{r^4} \tilde{\Psi}_{2\pm2}^{(o)}(\omega; r) = 0. \quad (A20)$$

From these equations, we find the "Chandrasekhar" transformation as

$$\tilde{\Psi}_{2\pm2}^{(o)}(\omega; r) = \left(6 + 9 \frac{M^2(r-2M)}{r^2(2r+3M)} \mp \frac{SM\omega(45M^2 - 48r^2)}{r^2(2r+3M)^2} \right)$$
$$\times \tilde{\Psi}_{2\pm2}(\omega; r) + 3M\left(1 - 2\frac{M}{r}\right)\left(1 \pm \frac{4}{3}\frac{S\omega}{M}\right)$$
$$\times \frac{d}{dr} \tilde{\Psi}_{2\pm2}(\omega; r). \quad (A21)$$

TABLE VI. The quasinormal frequencies in terms of $\rho = -i\omega$. The $m = -2$ mode can be considered as the $m = 2$ mode with the inverse spin signature. Here we set $a_{17} = 0$ in the recurrence relation of Eq. (A26). This creates the numerical error in our calculation (see $\chi = 0.0$).

| χ	$m = 2$ (This paper)	$m = 2$ ([68])	$\text{Err}_{\Re}$	$\text{Err}_{\Im}$
-0.9	$-0.173\,072 - 0.581\,783i$	$-0.176\,562 - 0.594\,488i$	$-0.019\,766$	$0.021\,371$
-0.8	$-0.174\,141 - 0.595\,877i$	$-0.177\,024 - 0.606\,626i$	$-0.016\,285$	$0.017\,719$
-0.7	$-0.175\,137 - 0.610\,783i$	$-0.177\,434 - 0.619\,616i$	$-0.012\,945$	$0.014\,255$
-0.6	$-0.176\,039 - 0.626\,584i$	$-0.177\,784 - 0.633\,568i$	$-0.009\,815$	$0.011\,023$
-0.5	$-0.176\,825 - 0.643\,379i$	$-0.178\,062 - 0.648\,614i$	$-0.006\,947$	$0.008\,071$
-0.4	$-0.177\,466 - 0.661\,283i$	$-0.178\,262 - 0.664\,916i$	$-0.004\,465$	$0.005\,463$
-0.3	$-0.177\,930 - 0.680\,440i$	$-0.178\,368 - 0.682\,666i$	$-0.002\,455$	$0.003\,260$
-0.2	$-0.178\,181 - 0.701\,019i$	$-0.178\,364 - 0.702\,106i$	$-0.001\,025$	$0.001\,548$
-0.1	$-0.178\,186 - 0.723\,233i$	$-0.178\,228 - 0.723\,536i$	$-0.000\,235$	$0.000\,418$
0.0	$-0.177\,923 - 0.747\,340i$	$-0.177\,924 - 0.747\,344i$	$-0.000\,005$	$0.000\,005$
0.1	$-0.177\,398 - 0.773\,654i$	$-0.177\,412 - 0.774\,036i$	$-0.000\,078$	$0.000\,493$
0.2	$-0.176\,662 - 0.802\,534i$	$-0.176\,622 - 0.804\,290i$	$0.000\,226$	$0.002\,183$
0.3	$-0.175\,836 - 0.834\,372i$	$-0.175\,458 - 0.839\,054i$	$0.002\,154$	$0.005\,580$
0.4	$-0.175\,116 - 0.869\,549i$	$-0.173\,764 - 0.879\,684i$	$0.007\,780$	$0.011\,521$
0.5	$-0.174\,747 - 0.908\,398i$	$-0.171\,278 - 0.928\,246i$	$0.020\,253$	$0.021\,382$
0.6	$-0.174\,999 - 0.951\,162i$	$-0.167\,532 - 0.988\,090i$	$0.044\,570$	$0.037\,373$
0.7	$-0.176\,094 - 0.997\,991i$	$-0.161\,588 - 1.065\,198i$	$0.089\,771$	$0.063\,095$
0.8	$-0.178\,154 - 1.048\,919i$	$-0.151\,252 - 1.172\,030i$	$0.177\,862$	$0.105\,040$
0.9	$-0.181\,181 - 1.103\,919i$	$-0.129\,726 - 1.343\,268i$	$0.396\,644$	$0.178\,185$
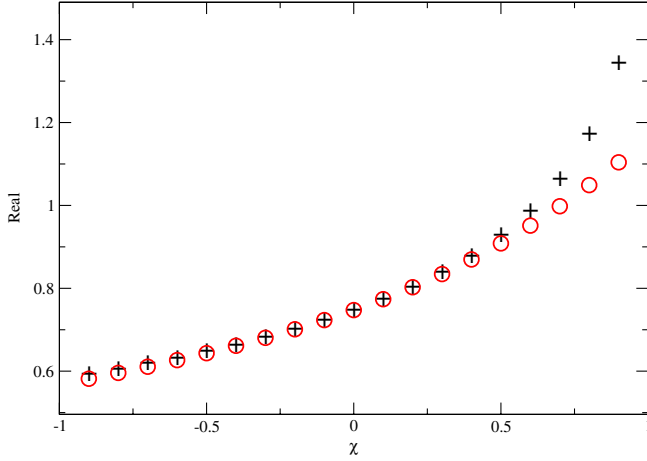
FIG. 29 (color online). The real part of the quasinormal frequencies, ω for $-0.9 \leq \chi \leq 0.9$. The horizontal axis denotes the nondimensional spin parameter, $\chi = S/M^2$. The (red) circles show our result, and the $+$ marks denote the values given in Table II of [68].

The differential equations for the even and odd parity perturbation become the same form by using the above transformation.

Next, we consider quasinormal modes derived from Eq. (A20). A recent review for quasinormal modes is given in [66]. Here, we should note that if we use Eq. (A18) to obtain the simple equation in Eq. (A20), these change the boundary behaviors near the horizon and at infinity. Therefore, although the expression is same in the $O(a^1)$ expansion, we should consider doing another transformation:
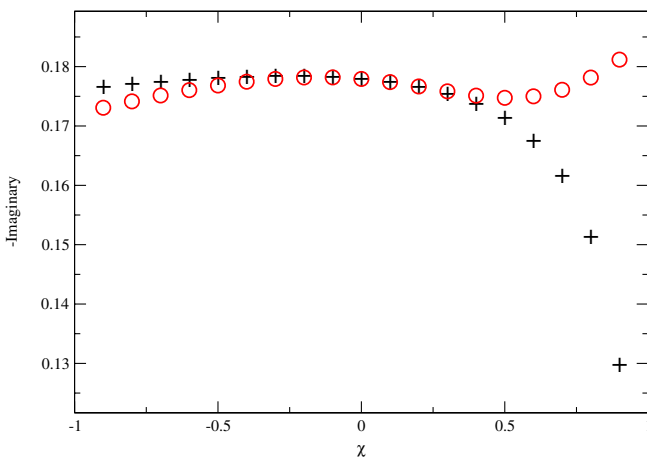

FIG. 30 (color online). The (minus) imaginary part of the quasinormal frequencies, ω for $-0.9 \leq \chi \leq 0.9$. The horizontal axis denotes the nondimensional spin parameter, $\chi = S/M^2$. The (red) circles show our result, and the $+$ marks denote the values given in Table II of [68].

$$\Psi_{2\pm2}^{(o)}(\omega; r)$$
$$= \left[1 + \frac{r - 2M}{r} \ln\left(1 \pm \frac{S\omega r}{(r - 2M)^2}\right)\right] \tilde{\Psi}_{2\pm2}^{(o)}(\omega; r).$$
$$\text{(A22)}$$

This does not change the boundary behaviors.

In order to calculate the quasinormal frequencies, we use the Leaver's method [67]. As boundary conditions, the wave function $\tilde{\Psi}_{2\pm2}^{(o)}$ has the following behaviors:

$$\tilde{\Psi}_{2\pm2}^{(o)}(\rho; r) \rightarrow r^{-\rho} e^{-\rho r} \quad \text{for } r \rightarrow \infty,$$
$$\tilde{\Psi}_{2\pm2}^{(o)}(\rho; r) \rightarrow (r - 1)^{\rho + i\chi} \quad \text{for } r \rightarrow 1,$$
$$\text{(A23)}$$

where we have considered $2M = 1$ and $\rho = -i\omega$ which are the same notation as [67]. Here, χ is defined by the nondimensional spin parameter $\chi = S/M^2$. Then a solution of Eq. (A20) can be written in the form of

$$\tilde{\Psi}_{2\pm2}^{(o)}(\rho; r) = r^{-\rho} e^{-\rho(r-1)} (r - 1)^{\rho + i\chi} r^{-(\rho + i\chi)}$$
$$\times \sum_{n=0}^{\infty} a_n \left(\frac{r - 1}{r}\right)^n. \quad \text{(A24)}$$

We obtain the recurrence relation for a_n in the above equation,

$$\alpha_0 a_1 + \beta_0 a_0 = 0, \quad \text{(A25)}$$

and for $n \geq 1$,

$$\alpha_n a_{n+1} + \beta_n a_n + \gamma_n a_{n-1} = 0, \quad \text{(A26)}$$
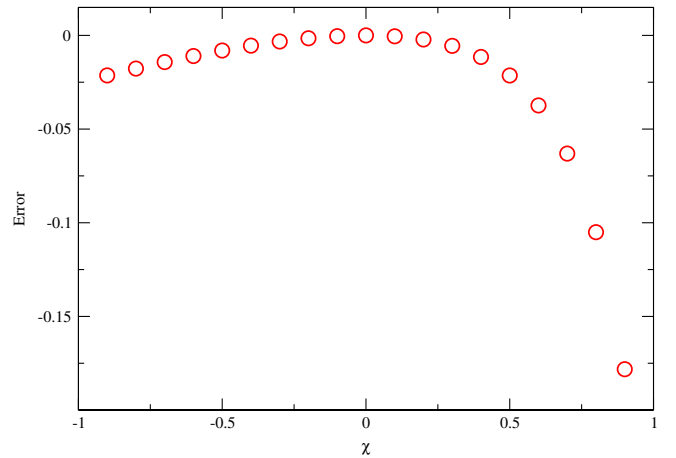
where

FIG. 31 (color online). The error in the real part of the quasinormal frequencies, i.e., $-\text{Err}_{\tilde{\omega}}$. The horizontal axis denotes the nondimensional spin parameter, $\chi = S/M^2$.
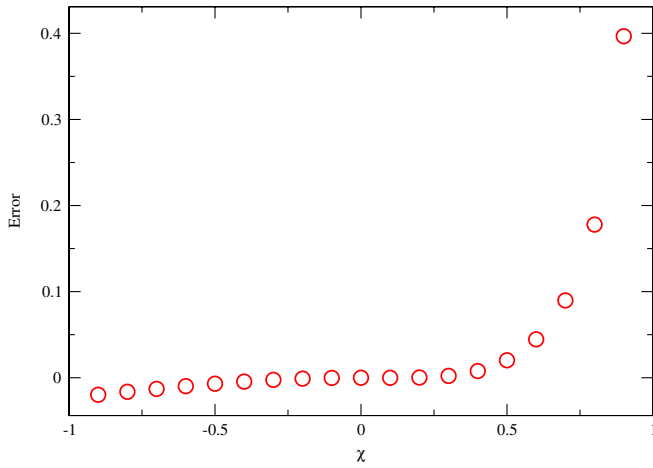
FIG. 32 (color online).   The error in the (minus) imaginary part of the quasinormal frequencies, i.e., $\text{Err}_{\mathfrak{R}}$. The horizontal axis denotes the nondimensional spin parameter, $\chi = S/M^2$.

$$\alpha_n = (2 + 2n)\rho + 2i(n + 1)\chi + (n + 1)^2,$$

$$\beta_n = -8\rho^2 + (-4 - 8n - 7i\chi)\rho$$
$$- 2i(2n + 1)\chi - 3 - 2n^2 - 2n,$$

$$\gamma_n = 4\rho^2 + (4n + 5i\chi)\rho + 2i\chi n + (n - 2)(n + 2).$$

$$(A27)$$

When we set $\chi = 0$, the above equations reduce to Eq. (8) in [67].

In Fig. 25, we show the result for the quasinormal frequencies, ω around $\chi = 0$. As a reference, we also plot the values given in Table II of [68]. Figures 26 and 27 show the real and imaginary parts of the quasinormal frequencies around $\chi = 0$, respectively. Figures 28–30
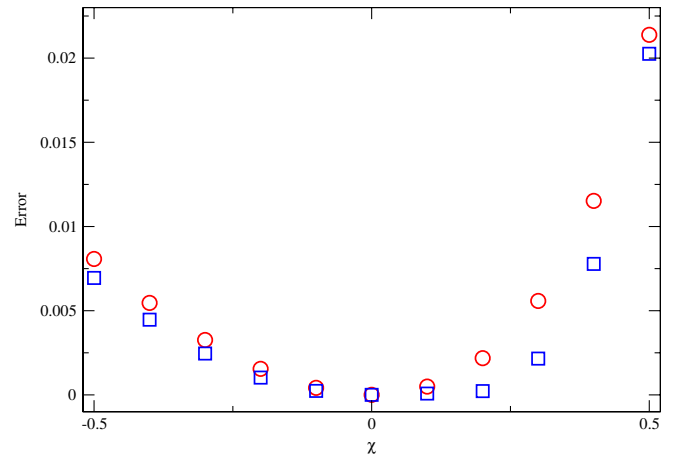

FIG. 33 (color online).   The absolute value of the relative errors in quasinormal frequencies in the region $-0.5 \leq \chi \leq 0.5$. The (red) circles and (blue) boxes show those of the real and imaginary parts of the frequencies, i.e., $|\text{Err}_{\mathfrak{I}}|$ and $|\text{Err}_{\mathfrak{R}}|$, respectively. The horizontal axis denotes the nondimensional spin parameter, $\chi = S/M^2$.

show the result for $-0.9 \leq \chi \leq 0.9$. In Table VI, we show the numerical values and the relative errors for the real and imaginary parts of ρ defined by

$$\text{Err}_{\mathfrak{R}} = \frac{\mathfrak{R}(\rho_a) - \mathfrak{R}(\rho)}{\mathfrak{R}(\rho)}, \quad \text{Err}_{\mathfrak{I}} = \frac{\mathfrak{I}(\rho_a) - \mathfrak{I}(\rho)}{\mathfrak{I}(\rho)}, \quad (A28)$$

where ρ_a and ρ represent our result and that of [68], respectively. We plot the above errors in Figs. 31 and 32, and we zoom in on the region $-0.5 \leq \chi \leq 0.5$ in Fig. 33 which shows the absolute values of the relative error.

[1] M. Volonteri and P. Madau, Astrophys. J. **687**, L57 (2008).
[2] D. A. Brown *et al.*, Phys. Rev. Lett. **99**, 201102 (2007).
[3] I. Mandel, D. A. Brown, J. R. Gair, and M. C. Miller, Astrophys. J. **681**, 1431 (2008).
[4] I. Mandel and J. R. Gair, Classical Quantum Gravity **26**, 094036 (2009).
[5] M. Campanelli, C. O. Lousto, P. Marronetti, and Y. Zlochower, Phys. Rev. Lett. **96**, 111101 (2006).
[6] J. G. Baker, J. Centrella, D.-I. Choi, M. Koppitz, and J. van Meter, Phys. Rev. Lett. **96**, 111102 (2006).
[7] F. Pretorius, Phys. Rev. Lett. **95**, 121101 (2005).
[8] M. Campanelli, C. O. Lousto, Y. Zlochower, and D. Merritt, Astrophys. J. **659**, L5 (2007).
[9] M. Campanelli, C. O. Lousto, H. Nakano, and Y. Zlochower, Phys. Rev. D **79**, 084010 (2009).
[10] B. Szilagyi, L. Lindblom, and M. A. Scheel, Phys. Rev. D **80**, 124010 (2009).
[11] C. O. Lousto, H. Nakano, Y. Zlochower, and M. Campanelli, Phys. Rev. Lett. **104**, 211101 (2010).
[12] C. O. Lousto and Y. Zlochower, arXiv:1009.0292.
[13] S. Brandt and B. Brügmann, Phys. Rev. Lett. **78**, 3606 (1997).
[14] M. Ansorg, B. Brügmann, and W. Tichy, Phys. Rev. D **70**, 064011 (2004).
[15] Y. Zlochower, J. G. Baker, M. Campanelli, and C. O. Lousto, Phys. Rev. D **72**, 024021 (2005).
[16] P. Marronetti, W. Tichy, B. Brügmann, J. Gonzalez, and U. Sperhake, Phys. Rev. D **77**, 064010 (2008).
[17] C. O. Lousto and Y. Zlochower, Phys. Rev. D **77**, 024034 (2008).
[18] E. Schnetter, S. H. Hawley, and I. Hawke, Classical Quantum Gravity **21**, 1465 (2004).
[19] J. Thornburg, Classical Quantum Gravity **21**, 743 (2004).

[20] O. Dreyer, B. Krishnan, D. Shoemaker, and E. Schnetter, Phys. Rev. D **67**, 024018 (2003).

[21] M. Campanelli, C. O. Lousto, Y. Zlochower, B. Krishnan, and D. Merritt, Phys. Rev. D **75**, 064030 (2007).

[22] M. Campanelli and C. O. Lousto, Phys. Rev. D **59**, 124022 (1999).

[23] C. O. Lousto and Y. Zlochower, Phys. Rev. D **76**, 041502 (R) (2007).

[24] M. Alcubierre, B. Brügmann, P. Diener, M. Koppitz, D. Pollney, E. Seidel, and R. Takahashi, Phys. Rev. D **67**, 084023 (2003).

[25] D. Mueller and B. Bruegmann, Classical Quantum Gravity **27**, 114008 (2010).

[26] E. Schnetter, Classical Quantum Gravity **27**, 167001 (2010).

[27] M. Alcubierre *et al.*, arXiv:gr-qc/0411137.

[28] D. Alic, L. Rezzolla, I. Hinder, and P. Mosta, arXiv:1008.2212.

[29] D. Muller, J. Grigsby, and B. Bruegmann, Phys. Rev. D **82**, 064004 (2010).

[30] H. P. Pfeiffer *et al.*, Classical Quantum Gravity **24**, S59 (2007).

[31] C. O. Lousto, Classical Quantum Gravity **22**, S543 (2005).

[32] H. Nakano and K. Ioka, Phys. Rev. D **76**, 084007 (2007).

[33] Y. Mino, Phys. Rev. D **77**, 044008 (2008).

[34] C. O. Lousto and H. Nakano, Classical Quantum Gravity **26**, 015007 (2009).

[35] M. Hannam, S. Husa, D. Pollney, B. Brügmann, and N. O'Murchadha, Phys. Rev. Lett. **99**, 241102 (2007).

[36] B. Brügmann, Gen. Relativ. Gravit. **41**, 2131 (2009).

[37] T. Regge and J. A. Wheeler, Phys. Rev. **108**, 1063 (1957).

[38] F. J. Zerilli, Phys. Rev. D **2**, 2141 (1970).

[39] V. Moncrief, Ann. Phys. (N.Y.) **88**, 323 (1974).

[40] C. T. Cunningham, R. H. Price, and V. Moncrief, Astrophys. J. **224**, 643 (1978).

[41] R. J. Gleiser and A. E. Dominguez, Phys. Rev. D **65**, 064018 (2002).

[42] D. Brown *et al.*, arXiv:0709.0093.

[43] M. Bruni, S. Matarrese, S. Mollerach, and S. Sonego, Classical Quantum Gravity **14**, 2585 (1997).

[44] C. O. Lousto, Classical Quantum Gravity **22**, S569 (2005).

[45] C. Reisswig, N. T. Bishop, D. Pollney, and B. Szilagyi, Phys. Rev. Lett. **103**, 221101 (2009).

[46] D. Pollney, C. Reisswig, E. Schnetter, N. Dorband, and P. Diener, arXiv:0910.3803.

[47] C. O. Lousto and R. H. Price, Phys. Rev. D **56**, 6439 (1997).

[48] G. Khanna and J. McKennon, Comput. Phys. Commun. **181**, 1605 (2010).

[49] C. Reisswig and D. Pollney, arXiv:1006.1632.

[50] P. A. Sundararajan, G. Khanna, and S. A. Hughes, Phys. Rev. D **81**, 104009 (2010).

[51] C. O. Lousto, M. Campanelli, Y. Zlochower, and H. Nakano, Classical Quantum Gravity **27**, 114006 (2010).

[52] C. O. Lousto, H. Nakano, Y. Zlochower, and M. Campanelli, Phys. Rev. D **81**, 084023 (2010).

[53] R. Arnowitt, S. Deser, and C. W. Misner, Phys. Rev. **118**, 1100 (1960).

[54] A. Buonanno, Y. Chen, and T. Damour, Phys. Rev. D **74**, 104005 (2006).

[55] A. Buonanno and T. Damour, Phys. Rev. D **59**, 084006 (1999).

[56] Y. Pan *et al.*, Phys. Rev. D **81**, 084041 (2010).

[57] A. Nagar, T. Damour, and A. Tartaglia, Classical Quantum Gravity **24**, S109 (2007).

[58] T. Damour and A. Nagar, Phys. Rev. D **76**, 064028 (2007).

[59] S. Bernuzzi and A. Nagar, Phys. Rev. D **81**, 084056 (2010).

[60] J. Baker, M. Campanelli, C. O. Lousto, and R. Takahashi, Phys. Rev. D **65**, 124012 (2002).

[61] M. Campanelli, C. O. Lousto, and Y. Zlochower, Phys. Rev. D **73**, 061501(R) (2006).

[62] J. G. Baker, J. Centrella, D.-I. Choi, M. Koppitz, and J. van Meter, Phys. Rev. D **73**, 104002 (2006).

[63] I. Hinder, B. Vaishnav, F. Herrmann, D. Shoemaker, and P. Laguna, Phys. Rev. D **77**, 081502 (2008).

[64] S. Chandrasekhar, *The Mathematical Theory of Black Holes* (Oxford University Press, Oxford, England, 1983).

[65] L. Barack and N. Sago, Phys. Rev. Lett. **102**, 191101 (2009).

[66] E. Berti, V. Cardoso, and A. O. Starinets, Classical Quantum Gravity **26**, 163001 (2009).

[67] E. W. Leaver, Proc. R. Soc. A **402**, 285 (1985).

[68] K. Glampedakis and N. Andersson, Classical Quantum Gravity **20**, 3441 (2003).